# X-Ray Polarization of the Black Hole X-Ray Binary 4U 1630–47 Challenges the Standard Thin Accretion Disk Scenario

Ajay Ratheesh, Michal Dovčiak, Henric Krawczynski, Jakub Podgorný, Lorenzo Marra, Alexandra Veledina, Valery F. Suleimanov, Nicole Rodriguez Cavero, James F. Steiner, Jiří Svoboda, et al.

The Astrophysical Journal, 964:77 (20pp), 2024 March 20 https://doi.org/10.3847/1538-4357/ad226e


# X-Ray Polarization of the Black Hole X-Ray Binary 4U 1630–47 Challenges the Standard Thin Accretion Disk Scenario

Ajay Ratheesh[1], Michal Dovčiak[2], Henric Krawczynski[3], Jakub Podgorný[2,4,5], Lorenzo Marra[6], Alexandra Veledina[7,8], Valery F. Suleimanov[9], Nicole Rodriguez Cavero[3], James F. Steiner[10], Jiří Svoboda[2], Andrea Marinucci[11], Stefano Bianchi[6], Michela Negro[12,13,14], Giorgio Matt[6], Francesco Tombesi[15,16,17], Juri Poutanen[7], Adam Ingram[18], Roberto Taverna[19], Andrew West[3], Vladimir Karas[2], Francesco Ursini[6], Paolo Soffitta[1], Fiamma Capitanio[1], Domenico Viscolo[20], Alberto Manfreda[21], Fabio Muleri[1], Maxime Parra[6,22], Banafsheh Beheshtipour[3], Sohee Chun[3], Nicolò Cibrario[23,24], Niccolò Di Lalla[25], Sergio Fabiani[1], Kun Hu[3], Philip Kaaret[26], Vladislav Loktev[7], Romana Mikušincová[6], Tsunefumi Mizuno[27], Nicola Omodei[25], Pierre-Olivier Petrucci[22], Simonetta Puccetti[28], John Rankin[1], Silvia Zane[29], Sixuan Zhang[27], Iván Agudo[30], Lucio A. Antonelli[28,31], Matteo Bachetti[32], Luca Baldini[20,33], Wayne H. Baumgartner[26], Ronaldo Bellazzini[20], Stephen D. Bongiorno[26], Raffaella Bonino[23,24], Alessandro Brez[20], Niccolò Bucciantini[34,35,36], Simone Castellano[20], Elisabetta Cavazzuti[11], Chien-Ting Chen[37], Stefano Ciprini[16,28], Enrico Costa[1], Alessandra De Rosa[1], Ettore Del Monte[1], Laura Di Gesu[11], Alessandro Di Marco[1], Immacolata Donnarumma[11], Victor Doroshenko[9], Steven R. Ehlert[26], Teruaki Enoto[38], Yuri Evangelista[1], Riccardo Ferrazzoli[1], Javier A. Garcia[39], Shuichi Gunji[40], Kiyoshi Hayashida[41], Jeremy Heyl[42], Wataru Iwakiri[43], Svetlana G. Jorstad[44,45], Fabian Kislat[46], Takao Kitaguchi[38], Jeffery J. Kolodziejczak[26], Fabio La Monaca[1], Luca Latronico[23], Ioannis Liodakis[47], Simone Maldera[23], Frédéric Marin[4], Alan P. Marscher[44], Herman L. Marshall[48], Francesco Massaro[23,24], Ikuyuki Mitsuishi[49], Stephen C.-Y. Ng[50], Stephen L. O'Dell[26], Chiara Oppedisano[23], Alessandro Papitto[31], George G. Pavlov[51], Abel L. Peirson[25], Matteo Perri[28,31], Melissa Pesce-Rollins[20], Maura Pilia[32], Andrea Possenti[32], Brian D. Ramsey[26], Oliver J. Roberts[37], Roger W. Romani[25], Carmelo Sgrò[20], Patrick Slane[10], Gloria Spandre[20], Douglas A. Swartz[37], Toru Tamagawa[38], Fabrizio Tavecchio[52], Yuzuru Tawara[49], Allyn F. Tennant[26], Nicholas E. Thomas[26], Alessio Trois[32], Sergey S. Tsygankov[7], Roberto Turolla[19,29], Jacco Vink[53], Martin C. Weisskopf[26], Kinwah Wu[29], and Fei Xie[1,54]

[1] INAF Istituto di Astrofisica e Planetologia Spaziali, Via del Fosso del Cavaliere 100, 00133 Roma, Italy; ajay.ratheesh@inaf.it
[2] Astronomical Institute of the Czech Academy of Sciences, Boční II 1401/1, 14100 Praha 4, Czech Republic
[3] Physics Department and McDonnell Center for the Space Sciences, Washington University in St. Louis, St. Louis, MO 63130, USA
[4] Université de Strasbourg, CNRS, Observatoire Astronomique de Strasbourg, UMR 7550, 67000 Strasbourg, France
[5] Astronomical Institute, Charles University, V Holešovičkách 2, CZ-18000, Prague, Czech Republic
[6] Dipartimento di Matematica e Fisica, Università degli Studi Roma Tre, Via della Vasca Navale 84, 00146 Roma, Italy
[7] Department of Physics and Astronomy, 20014 University of Turku, Finland
[8] Nordita, KTH Royal Institute of Technology and Stockholm University, Hannes Alfvéns väg 12, SE-10691 Stockholm, Sweden
[9] Institut für Astronomie und Astrophysik, Universität Tübingen, Sand 1, 72076 Tübingen, Germany
[10] Center for Astrophysics| Harvard & Smithsonian, 60 Garden Street, Cambridge, MA 02138, USA
[11] ASI—Agenzia Spaziale Italiana, Via del Politecnico snc, 00133 Roma, Italy
[12] University of Maryland, Baltimore County, Baltimore, MD 21250, USA
[13] NASA Goddard Space Flight Center, Greenbelt, MD 20771, USA
[14] Center for Research and Exploration in Space Science and Technology, NASA/GSFC, Greenbelt, MD 20771, USA
[15] Dipartimento di Fisica, Università degli Studi di Roma "Tor Vergata", Via della Ricerca Scientifica 1, 00133 Roma, Italy
[16] Istituto Nazionale di Fisica Nucleare, Sezione di Roma "Tor Vergata", Via della Ricerca Scientifica 1, 00133 Roma, Italy
[17] Department of Astronomy, University of Maryland, College Park, MD 20742, USA
[18] School of Mathematics, Statistics, and Physics, Newcastle University, Newcastle upon Tyne NE1 7RU, UK
[19] Dipartimento di Fisica e Astronomia, Università degli Studi di Padova, Via Marzolo 8, 35131 Padova, Italy
[20] Istituto Nazionale di Fisica Nucleare, Sezione di Pisa, Largo B. Pontecorvo 3, 56127 Pisa, Italy
[21] Istituto Nazionale di Fisica Nucleare, Sezione di Napoli, Strada Comunale Cinthia, 80126 Napoli, Italy
[22] Université Grenoble Alpes, CNRS, IPAG, 38000 Grenoble, France
[23] Istituto Nazionale di Fisica Nucleare, Sezione di Torino, Via Pietro Giuria 1, 10125 Torino, Italy
[24] Dipartimento di Fisica, Università degli Studi di Torino, Via Pietro Giuria 1, 10125 Torino, Italy
[25] Department of Physics and Kavli Institute for Particle Astrophysics and Cosmology, Stanford University, Stanford, CA 94305, USA
[26] NASA Marshall Space Flight Center, Huntsville, AL 35812, USA
[27] Hiroshima Astrophysical Science Center, Hiroshima University, 1-3-1 Kagamiyama, Higashi-Hiroshima, Hiroshima 739-8526, Japan
[28] Space Science Data Center, Agenzia Spaziale Italiana, Via del Politecnico snc, 00133 Roma, Italy
[29] Mullard Space Science Laboratory, University College London, Holmbury St Mary, Dorking, Surrey RH5 6NT, UK
[30] Instituto de Astrofísica de Andalucía–CSIC, Glorieta de la Astronomía s/n, 18008 Granada, Spain
[31] INAF Osservatorio Astronomico di Roma, Via Frascati 33, 00078 Monte Porzio Catone (RM), Italy
[32] INAF Osservatorio Astronomico di Cagliari, Via della Scienza 5, 09047 Selargius (CA), Italy
[33] Dipartimento di Fisica, Università di Pisa, Largo B. Pontecorvo 3, 56127 Pisa, Italy
[34] INAF Osservatorio Astrofisico di Arcetri, Largo Enrico Fermi 5, 50125 Firenze, Italy
[35] Dipartimento di Fisica e Astronomia, Università degli Studi di Firenze, Via Sansone 1, 50019 Sesto Fiorentino (FI), Italy
[36] Istituto Nazionale di Fisica Nucleare, Sezione di Firenze, Via Sansone 1, 50019 Sesto Fiorentino (FI), Italy
[37] Science and Technology Institute, Universities Space Research Association, Huntsville, AL 35805, USA
[38] RIKEN Cluster for Pioneering Research, 2-1 Hirosawa, Wako, Saitama 351-0198, Japan
[39] California Institute of Technology, Pasadena, CA 91125, USA
[40] Yamagata University, 1-4-12 Kojirakawa-machi, Yamagata-shi 990-8560, Japan

[41] Osaka University, 1-1 Yamadaoka, Suita, Osaka 565-0871, Japan
[42] University of British Columbia, Vancouver, BC V6T 1Z4, Canada
[43] International Center for Hadron Astrophysics, Chiba University, Chiba 263-8522, Japan
[44] Institute for Astrophysical Research, Boston University, 725 Commonwealth Avenue, Boston, MA 02215, USA
[45] Department of Astrophysics, St. Petersburg State University, Universitetsky pr. 28, Petrodvoretz, 198504 St. Petersburg, Russia
[46] Department of Physics and Astronomy and Space Science Center, University of New Hampshire, Durham, NH 03824, USA
[47] Finnish Centre for Astronomy with ESO, 20014 University of Turku, Finland
[48] MIT Kavli Institute for Astrophysics and Space Research, Massachusetts Institute of Technology, 77 Massachusetts Avenue, Cambridge, MA 02139, USA
[49] Graduate School of Science, Division of Particle and Astrophysical Science, Nagoya University, Furo-cho, Chikusa-ku, Nagoya, Aichi 464-8602, Japan
[50] Department of Physics, The University of Hong Kong, Pokfulam, Hong Kong
[51] Department of Astronomy and Astrophysics, Pennsylvania State University, University Park, PA 16802, USA
[52] INAF Osservatorio Astronomico di Brera, Via E. Bianchi 46, 23807 Merate (LC), Italy
[53] Anton Pannekoek Institute for Astronomy & GRAPPA, University of Amsterdam, Science Park 904, 1098 XH Amsterdam, The Netherlands
[54] Guangxi Key Laboratory for Relativistic Astrophysics, School of Physical Science and Technology, Guangxi University, Nanning 530004, People's Republic of China

*Received 2023 July 6; revised 2023 December 27; accepted 2024 January 19; published 2024 March 18*

## Abstract

A large energy-dependent X-ray polarization degree is detected by the Imaging X-ray Polarimetry Explorer (IXPE) in the high-soft emission state of the black hole X-ray binary 4U 1630–47. The highly significant detection (at $\approx 50\sigma$ confidence level) of an unexpectedly high polarization, rising from $\sim$6% at 2 keV to $\sim$10% at 8 keV, cannot be easily reconciled with standard models of thin accretion disks. In this work, we compare the predictions of different theoretical models with the IXPE data and conclude that the observed polarization properties are compatible with a scenario in which matter accretes onto the black hole through a thin disk covered by a partially ionized atmosphere flowing away at mildly relativistic velocities.

*Unified Astronomy Thesaurus concepts:* Polarimetry (1278); X-ray astronomy (1810); Stellar mass black holes (1611); Accretion (14)

## 1. Introduction

Black hole X-ray binaries (BHXRBs) consist of a black hole (BH) accreting matter from a companion star. These systems provide opportunities to investigate the inner workings of accretion flows, including their thermal stability and the mechanisms of angular momentum transport, as well as the formation of relativistic outflows, winds, and jets (Mészáros & Rees 1997; Fender 2001; Ponti et al. 2012).

The X-ray polarization observations (in the 2–8 keV range) conducted with the Imaging X-ray Polarimetry Explorer (IXPE; Weisskopf et al. 2022), a NASA mission in collaboration with the Italian Space Agency (ASI) launched on 2021 December 9, are providing us with new significant insights into BHXRBs. In particular, the 4% polarization observed for the archetypal BHXRB Cyg X-1 (Krawczynski et al. 2022), parallel to the radio jet, constrained the geometry of the hot corona responsible for the power-law emission in the hard state, to be extended perpendicular to the jet direction (see Remillard & McClintock 2006; Done et al. 2007, for detailed descriptions of the different X-ray states). IXPE monitored the polarization properties of the recently discovered BH binary candidate, Swift J1727.8−1613, throughout its state transition from a hard to a soft state, suggesting that the Comptonizing corona extends over the disk, similar to the case of Cyg X-1 (Veledina et al. 2023a; Ingram et al. 2023). In the disk-dominated spectral states of LMC X-1, LMC X-3, and 4U 1957+115, IXPE observations indicate that the polarization measurements are consistent with the standard geometrically thin, optically thick accretion disks (Marra et al. 2023; Podgorný et al. 2023; Svoboda et al. 2024). Furthermore, in the case of LMC X-3 and 4U 1957+115, these observations place constraints on the spin of the BH. On the other hand, the much higher polarization degree (PD; $\sim$20%) observed for the BH candidate Cyg X-3 in the hard state (Veledina et al. 2023b), with a polarization direction perpendicular to that of the discrete radio blobs, can be explained if radiation emitted by a highly luminous (but not directly visible) source is reflected off the funnel walls of obscuring matter.

In this paper, we present the results of spectropolarimetric observations of the accreting BH 4U 1630–47 with IXPE, accompanied by spectral observations with the Neutron Star Interior Composition Explorer (NICER) and Nuclear Spectroscopic Telescope Array (NuSTAR) missions, discussing a comparison with the predictions of different theoretical models. IXPE observed 4U 1630–47 in the high-soft state, in which the emission is believed to originate from a geometrically thin, optically thick accretion disk ($h/r \ll 1$ for the scale height $h$ of the disk at radius $r$), manifesting itself as a multitemperature blackbody (BB; Novikov & Thorne 1973; Shakura & Sunyaev 1973; Esin et al. 1997; McClintock & Remillard 2006). However, slim ($h/r \lesssim 0.4$) and thick ($0.4 < h/r \lesssim 1$) accretion disks have also been provided as possible interpretations in the case of high accretion rates (Abramowicz et al. 1988). The IXPE observations of 4U 1630–47 now allow us to weigh in on this distinction thanks to the additional information encoded in the energy-resolved PD and polarization direction.

4U 1630–47 is a transient low-mass X-ray binary system, initially discovered by the Uhuru satellite in 1969 (Giacconi et al. 1972; Priedhorsky 1986), that subsequently exhibited recurrent outbursts with a spacing of approximately 2–3 yr (Kuulkers et al. 1998; Capitanio et al. 2015). An accurate determination of the properties of the binary system has not been possible as yet due to the high line-of-sight (LOS) extinction (Reid et al. 1980; Parmar et al. 1986). The BH mass, distance to the binary system, and inclination (angle between

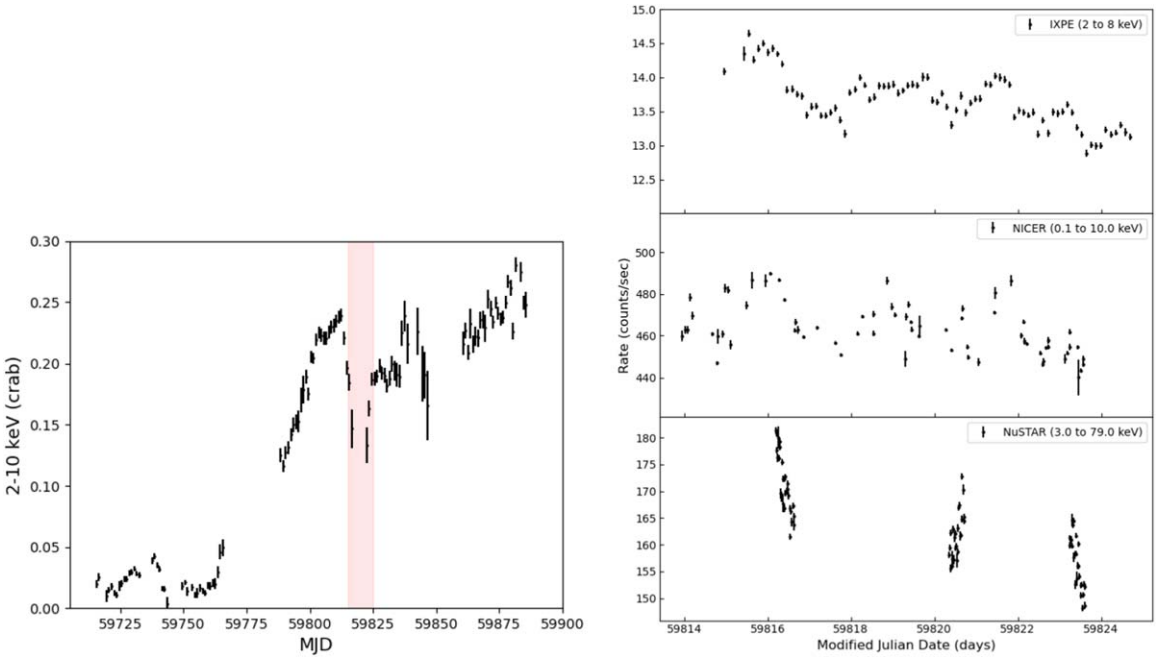


**Figure 1.** Left: MAXI 2–10 keV light curves in 1 day bins. The shaded red region indicates the time period of the IXPE observation campaign. Right: IXPE, NICER, and NuSTAR light curves in the 2–8, 0.1–10, and 3–79 keV bands, respectively, during the IXPE campaign. The IXPE light curve gives the combined count rates of all three DUs, whereas for NuSTAR, only the light curve obtained from the FPMA is shown.

the binary axis and the LOS) are thus poorly constrained. Based on the dust-scattering halo around the source, the distance is estimated to be between 4.7 and 11.5 kpc (Kalemci et al. 2018), while the inclination is believed to be $\sim 65^{\circ}$, explaining the observations of X-ray dips but the absence of eclipses (Kuulkers et al. 1998; Tomsick et al. 1998) and the detection of Doppler-shifted lines emitted by a jet (Díaz Trigo et al. 2014). The source shows evidence for a wind, believed to be equatorial (Díaz Trigo et al. 2014; King et al. 2014; Miller et al. 2015). The thermal component usually dominates the spectrum during outbursts (Parmar et al. 1986; Tomsick et al. 2005), making it an ideal candidate for investigating the properties of the disk.

We present the observational results in Section 2 and the theoretical modeling in Section 3. In Section 4, we compare the models to the data and conclude by discussing the implication of the results in Section 5.

## 2. Observational Results

Daily monitoring of 4U 1630–47 by the Gas Slit Camera on board Monitor of All-sky X-ray Image (MAXI; Matsuoka et al. 2009) showed an increase in the count rate, suggesting an outburst from the source in 2022 July (Jiang et al. 2022; see also Figure 1). During this outburst, IXPE performed a target-of-opportunity observation starting on 2022 August 23 and ending on 2022 September 2, for a total exposure of approximately 460 ks, along with continuous spectral monitoring from NICER (Arzoumanian et al. 2014) and NuSTAR (Harrison et al. 2013). In this section, we show the light curves and polarimetric and spectroscopic analysis of the source.

*Light curves.* The left panel of Figure 1 shows the X-ray activity of the source between MJD 59700 (2022 May 1) and MHD 59900 (2022 November 17) monitored by the MAXI mission. The 200 day interval includes the time period of the IXPE observation campaign. The source was detected in the high-soft state. The right panel shows the IXPE 2–8 keV, NICER 1–10 keV, and NuSTAR 3–79 keV fluxes. The fluxes varied by $\sim$10% below 10 keV and by 15%–20% above 10 keV. Hence, the flux of the source was rather stable during the campaign (red shaded region).

*Polarization*. Linear polarization was detected with a statistical confidence of around $50\sigma$ (Figure 2). The 2–8 keV PD and polarization angle (PA), measured east of north, are $8.32\% \pm 0.17\%$ and $17\overset{\circ}{.}8 \pm 0\overset{\circ}{.}6$, respectively (uncertainties at 68% confidence level). Whereas PD increases from approximately 6% at 2 keV to 10% at 8 keV, PA stays constant with energy within statistical accuracy (see the Table 1). The radio jet from this source has never been resolved, leaving us without a jet direction to compare with the X-ray PA. The data reduction and analysis techniques are outlined in Appendix A.

*Spectral fit with NICER and NuSTAR*. The NICER data reveal a featureless power density spectrum with fractional variability of less than 5% rms and a high disk temperature of $\sim$1.4 keV, showing that the source was in the high-soft state. The NICER energy spectra also exhibit blueshifted absorption lines, suggesting the existence of equatorial disk wind outflows with velocities $\approx 0.003c$ (with $c$ the speed of light).

As 4U 1630−47 is variable (see Figure 1), we fitted the NICER and NuSTAR energy spectra selecting quasi-simultaneous data sets. From the set of NICER observations, we used data with observational IDs 5501010104, 5501010108, and 5501010111, which match the same periods covered by NuSTAR observations with observational IDs 80802313002, 80802313004, and 80802313006, respectively. Henceforth, we denote these three observations as Obs 1, Obs 2, and Obs 3, respectively. For the spectral analysis, we used only NICER data with low background radiation (we avoided data during the South Atlantic Anomaly, SAA, passage).

*Spectral model 1 (SM1)*. Initially, we fit the NICER and NuSTAR spectra using a multitemperature BB (`diskbb`) and a power law (`po`) with galactic cold absorption (`tbabs`); we

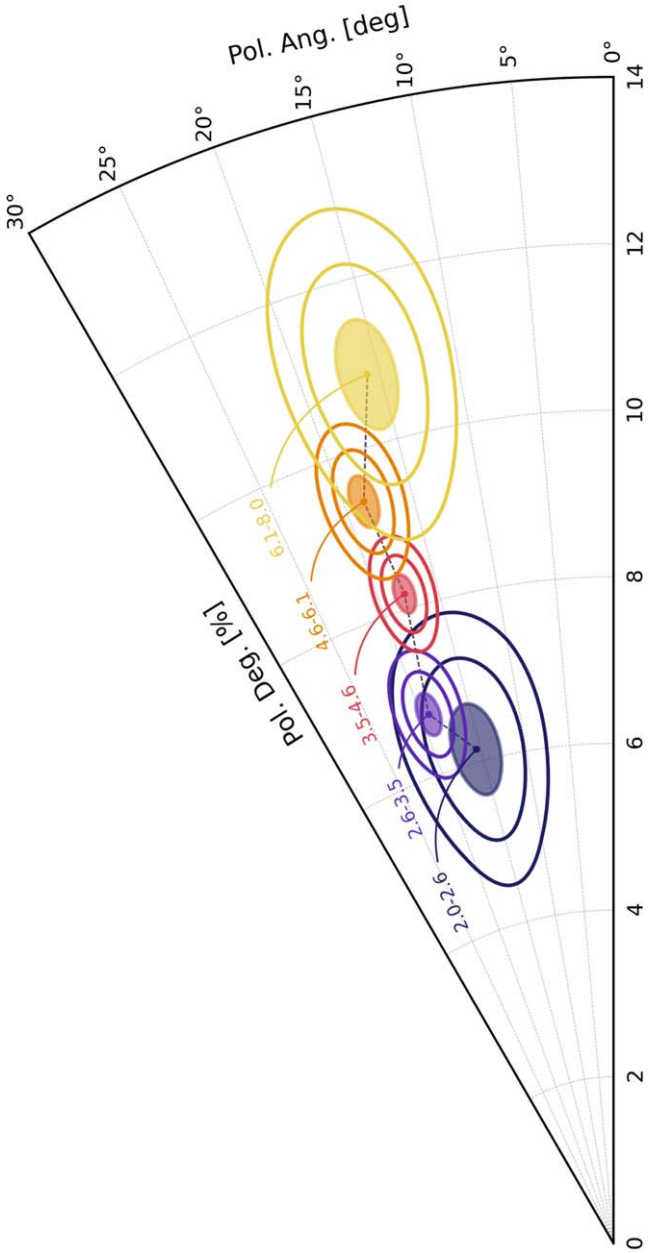


**Figure 2.** PD and PA measured for 4U 1630–47 as functions of the energy. The analysis is carried out using the publicly available version of `ixpeobssim` (Baldini et al. 2022). The shaded region and the ellipses show the 68% and the 95% and 99.7% confidence contours, respectively.

further used a constant to account for the calibration uncertainties between instruments. In XSPEC notation, this becomes `constant×tbabs×(diskbb+po)`. The power-law component was allowed to vary independently between observations. The fit resulted in an inner disk temperature of 1.38 keV and photon indices of 3.9, 4.1, and 4.3 for Obs 1, Obs 2, and Obs 3, respectively. However, the $\chi^2$/dof of the fit was 14692/2952, and hence not an acceptable fit. The fitted model and the fit residuals are shown in Figure 3.

*Spectral model 2 (SM2).* We then used a model consisting of thermal accretion disk emission accounting for relativistic effects (`kerrbb`; Li et al. 2005), the Comptonized emission `nthcomp` (Zdziarski et al. 1996; Życki et al. 1999), an ionized absorber modeled with `cloudy` (Ferland et al. 2017), and cold absorption `tbabs` (Wilms et al. 2000), accounting for Galactic

**Table 1**
PD and PA in Different Energy Bins across the IXPE 2–8 keV Band

| Energy Range (keV) | PD (%) | PA (deg) |
|---|---|---|
| 2.0–2.5 | $6.1 \pm 0.7$ | $14.6 \pm 3.3$ |
| 2.5–3.0 | $6.1 \pm 0.4$ | $17.8 \pm 1.9$ |
| 3.0–3.5 | $7.1 \pm 0.3$ | $19.8 \pm 1.3$ |
| 3.5–4.0 | $7.9 \pm 0.3$ | $17.8 \pm 1.2$ |
| 4.0–4.5 | $8.7 \pm 0.4$ | $18.3 \pm 1.2$ |
| 4.5–5.0 | $8.0 \pm 0.5$ | $16.3 \pm 1.7$ |
| 5.0–5.5 | $10.0 \pm 0.5$ | $18.8 \pm 1.5$ |
| 5.5–6.0 | $10.4 \pm 0.7$ | $18.4 \pm 1.9$ |
| 6.0–6.5 | $10.1 \pm 0.8$ | $19.3 \pm 2.3$ |
| 6.5–7.0 | $12.1 \pm 1.2$ | $12.8 \pm 2.7$ |
| 7.0–7.5 | $9.3 \pm 1.6$ | $14.3 \pm 4.9$ |
| 7.5–8.0 | $11.8 \pm 2.5$ | $18.9 \pm 6.0$ |

as well as local absorption. The `cloudy` absorption table reproduces the absorption lines self-consistently through a slab with a constant density of $10^{12}$ cm$^{-3}$ and a turbulence velocity of 500 km s$^{-1}$, illuminated by the unabsorbed intrinsic best-fit spectral energy distribution described below. Modeling the absorption lines requires a highly ionized outflowing plasma, i.e., with ionization parameter $\xi \sim 10^5$ and column density $N_{\rm Heq} \sim 10^{24}$ cm$^{-2}$. The seed photons for the `nthcomp` model are assumed to be from the multicolor-BB disk emission (inp_type parameter = 1), and we fixed the temperature to $kT_{\rm BB} = 1.38$ keV, as resulted from the initial fit (SM1). We further added an empirical `edge` model to account for the instrumental features at ≈2–3 keV in the NICER spectra and ≈10 keV in the NuSTAR spectra. The gold M edge in the NICER spectra is a well-known instrumental feature. We fixed the energy of the edge to the value $E = 2.4$ keV, as reported by Wang et al. (2021) in the analysis of MAXI J1820+070 NICER spectra. The origin of the ≈10 keV edge in the NuSTAR spectra is less known, but it was observed in other sources as well (e.g., the analysis of LMC X-1; Podgorný et al. 2023). We therefore modeled it with the empirical `edge` model. Finally, we accounted for absolute calibration uncertainties between the NICER and NuSTAR instruments, allowing for a small discrepancy in the spectral slope and normalization between the instruments using the `mbpo` model (see Krawczynski et al. 2022). This model can be denoted in XSPEC as `mbpo×edge×tbabs×cloudy×(kerrbb+nthcomp)`. The fitted model and the fit residuals are shown in Figure 3.

We further added a reflection component, a second Comptonization component, or a second ionized absorption component to the model, but none of these improved the overall fit or the residuals in this part of the NuSTAR spectrum.

With this model, we obtained the best fits for BH spins $a \gtrsim 0.99$, inclinations $i \approx 85°$, and masses $M_{\rm bh} \gtrsim 50\ M_\odot$ (Table 2, last line) with $\chi^2$/dof = 3563/2937. The mass is much higher than that (≈10 $M_\odot$) estimated from the previous analysis by Seifina et al. (2014).

As the BH mass, spin, inclination, and distance in the `kerrbb` model are degenerate, we fixed the distance of the source to $D_{\rm bh} = 11.5$ kpc (Kalemci et al. 2018). A smaller $D_{\rm bh}$ of 4.7 kpc is not excluded and would lead to a significantly smaller BH mass and accretion rate; e.g., for spin $a = 0.97$ and inclination $i = 75°$, the best-fit masses are $M_{\rm bh} \approx 26$ and 12 $M_\odot$, with effective accretion rates $M_{\rm dd} \approx 1.8 \times 10^{18}$ and $0.3 \times 10^{18}$ g s$^{-1}$ for $D_{\rm bh} = 11.5$ and 4.7 kpc, respectively. The best-fit value of the

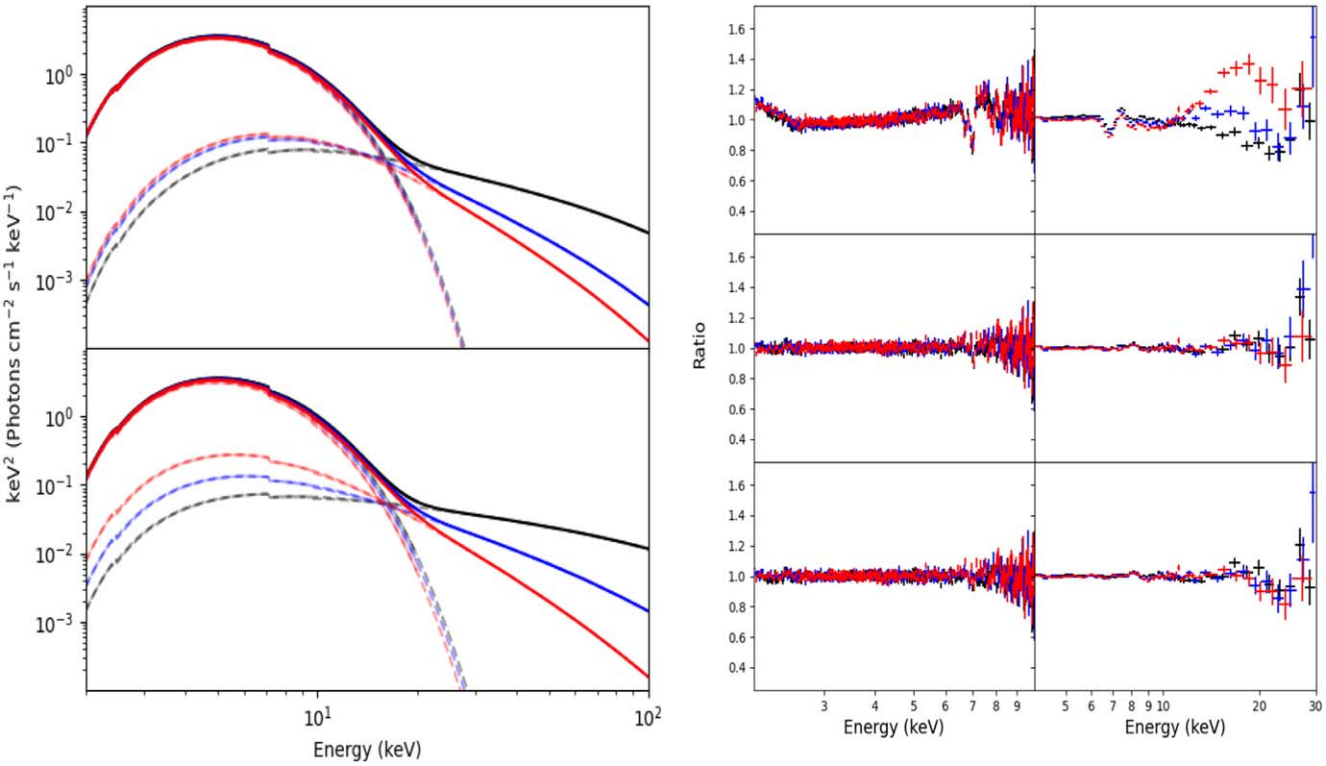


**Figure 3.** Left: the best-fit continuum models to the NICER and NuSTAR data using thermal accretion disk models `kerrbb` (top) and `slimbh` (bottom), along with the Comptonization component (`nthcomp`). The solid lines indicate the total model, while the dashed lines show the disk emission and Comptonization components. Right: the residuals (data/model) of the spectral fit NICER (left) and NuSTAR (right) data. The top, middle, and bottom panels represent the residuals from SM1, SM2, and SM3, respectively. Black, blue, and red correspond to Obs 1, Obs 2, and Obs 3, respectively.

**Table 2**
Spectral Fit Results for Different Fixed Values of BH Spin and Inclination with the `kerrbb` Model

| Inclination $i$ (deg) | Spin $a$ | Mass $M_{\rm bh}$ ($M_\odot$) | Accretion Rate $M_{\rm dd}$ ($10^{18}$ g s$^{-1}$) | Fit Goodness $\chi^2$ (2935 dof) |
|---|---|---|---|---|
| 70 | 0.7 | $9.98^{+0.06}_{-0.08}$ | 3.9–4.3 | 4693 |
| | 0.998 | $29.8^{+0.02}_{-0.02}$ | 0.99–1.09 | 3585 |
| 85 | 0.7 | $16.1^{+0.01}_{-0.01}$ | 8.3–8.9 | 3711 |
| | 0.998 | $59.8^{+0.04}_{-0.02}$ | 1.02–1.12 | 3563 |

BH mass is also impacted by the values of spin and inclination. Table 2 shows the mass and accretion rate results obtained with `kerrbb` for a fixed distance $D_{\rm bh} = 11.5$ kpc but for different sets of spin and inclination values. The goodness of the fit clearly shows the preference toward high masses.

*Spectral model 3 (SM3).* We then replaced `kerrbb` with the `slimbh` model (Sądowski 2011), which accounts for a vertical structure of the disk using the code `tlusty` (Hubeny & Hubeny 1998). This model is especially suited for high accretion rates and luminosities $L > 0.3\,L_{\rm Edd}$ when conditions for the razor-thin standard accretion disk model are not fulfilled and a very large hardening factor is required to well fit the spectra (Straub et al. 2011). In XSPEC notation, this model can be denoted as `mbpo×edge×tbabs×cloudy×(slimbh +nthcomp)`. The best-fit model describes the data with a $\chi^2/{\rm dof} = 3494/2933$ (see Figure 3 and Table 3). The reduced chi-squared value $\chi^2_{\rm red} = \chi^2/{\rm dof} \lesssim 1.2$ provides a very good fit, given that we have not applied any systematics to the data; these would account for uncertainties in the instrument calibration between NICER and NuSTAR (that can be within a few percent), as well as for possible spectral variability within the individual exposures (since the data acquired by the two missions were not strictly simultaneous).[55] Variable absorption lines are also a contributing factor to the chi-square in the joint spectral fits of NICER and NuSTAR. However, as it falls outside the main scope of our study, we did not delve into investigating this aspect in detail. It is noteworthy that these lines do not significantly impact the crucial continuum parameters in our analysis. The fit requires a BH mass of $\sim 18\,M_\odot$ and a spin $a \sim 0.7$, parameters that are more in line with expectations (Seifina et al. 2014). The luminosity is $L \approx 0.5\,L_{\rm Edd}$, i.e., already in the range in which the slim disk approximation is more appropriate than the geometrically thin disk one. The soft X-ray spectrum is dominated by the thermal accretion disk emission. NuSTAR data revealed a variable Comptonization component, which is most visible in a variable tail at very high energies (≈15–30 keV). The photon index varies in the range $\Gamma \approx 2.8$–$4.8$, while the soft X-ray spectrum varies only a bit. In the 2–8 keV energy range, the Comptonization contributes by 2%–3% and is almost negligible in the soft X-ray analysis.

We also investigated the time evolution of the spectral and polarimetric properties in 1 day bins. Here, we characterize the thermal component by its maximum temperature and normalization. Therefore, we base the spectral analysis on fitting the 2–10 keV NICER data with the multitemperature BB disk model (EZDISKBB; Zimmerman et al. 2005). We use the same CLOUDY model as in the main spectral fit to model the

[55] While we have restricted the NICER data to be within the NuSTAR observations, we did not do that vice versa, since the statistics of such restricted NuSTAR data would be too low.

**Table 3**
Spectral Fit Parameters to Simultaneous NICER and NuSTAR Observations with the `slimbh` Model

| Comp. | Parameter (unit) | Description | Obs 1 | Obs 2 | Obs 3 |
|---|---|---|---|---|---|
| `TBabs` | $N_{\rm H}$ ($10^{22}$ cm$^{-2}$) | H column density | $7.92^{+0.07}_{-0.02}$ | $7.94^{+0.02}_{-0.02}$ | $7.85^{+0.02}_{-0.02}$ |
| CLOUDY | $\log \xi$ | Ionization | $5.13^{+0.06}_{-0.04}$ | $5.01^{+0.09}_{-0.03}$ | $4.95^{+0.07}_{-0.04}$ |
| | $\log N_{\rm Heq}$ | H column density | $24.03^{+0.02}_{-0.02}$ | $24.03^{+0.03}_{-0.01}$ | $24.04^{+0.03}_{-0.02}$ |
| | $v$ (km s$^{-1}$) | Outflow velocity | <90 | $-900^{+300}_{-300}$ | $-900^{+300}_{-300}$ |
| `slimbh` | $M_{\rm bh}$ ($M_\odot$) | BH mass | | $18.0^{+0.7}_{-1.2}$ | |
| | $a$ | BH spin | | $0.71^{+0.03}_{-0.14}$ | |
| | $L_{\rm Edd}$ | Luminosity | $0.53^{+0.03}_{-0.03}$ | $0.51^{+0.02}_{-0.02}$ | $0.49^{+0.02}_{-0.02}$ |
| | $i$ (deg) | Inclination | | $85^{\rm f}_{-1.4}$ | |
| | $\alpha$ | Viscosity | | 0.1 (frozen) | |
| | $D_{\rm bh}$ (kpc) | Distance | | 11.5 (frozen) | |
| | hd | Hardening factor | | −1 (frozen) | |
| | $l_{\rm flag}$ | Limb-darkening | | 0 (frozen) | |
| | $v_{\rm flag}$ | Self-irradiation | | 0 (frozen) | |
| | norm | Normalization | | 1 (frozen) | |
| `nthcomp` | $\Gamma$ | Photon index | $2.6^{+0.2}_{-0.2}$ | $3.6^{+0.2}_{-0.2}$ | $4.5^{+0.2}_{-0.2}$ |
| | $kT_{\rm e}$ (keV) | Electron temp. | | 500 (frozen) | |
| | $kT_{\rm BB}$ (keV) | Seed photon temp. | | 1.47 (frozen) | |
| | norm ($10^{-2}$) | Normalization | $2.6^{+1.1}_{-0.7}$ | $6.3^{+1.8}_{-1.7}$ | $13^{+3}_{-3}$ |
| $\chi^2$/dof | | | | 3494/2933 | |

**Note.** The final model also included cross-calibration uncertainties between NICER and the NuSTAR A and B instruments, modeled by an `mbpo` model with $\Delta\Gamma = -0.101 \pm 0.008$ and normalization $N_{\rm mbpo} = 1.16 \pm 0.02$ (consistent for both NuSTAR A and B instruments), and the instrumental edges at $E = 2.4$ keV with maximum $\tau = 0.074 \pm 0.005$ for NICER and $E = 9.7 \pm 0.1$ keV with maximum $\tau = 0.056 \pm 0.006$ for NuSTAR. See the main text for more details.

absorption lines. We neglect the <2 keV data, since absorption strongly suppresses the low-energy flux. The thermal model gives a good fit, as the power-law component contributes only by 2%–3% to the 2–10 keV flux. The results of the analysis are shown in Figure 4. Whereas the maximum disk temperature stayed rather constant around ∼1.4 keV, the flux normalization varied between 35 and 40. The normalization is given by the expression $f^{-4}(R_{\rm in}/D)^2 \cos i$, where $f$ is the spectral hardening factor, $R_{\rm in}$ is the inner radius of the disk in kilometers, $D$ is the source distance in units of 10 kpc, and $i$ is the disk inclination. The PD shows significant variability. Fitting a constant model to the IXPE results gives a $\chi^2$ of 34.9 for 9 dof (chance probability $6 \times 10^{-5}$).

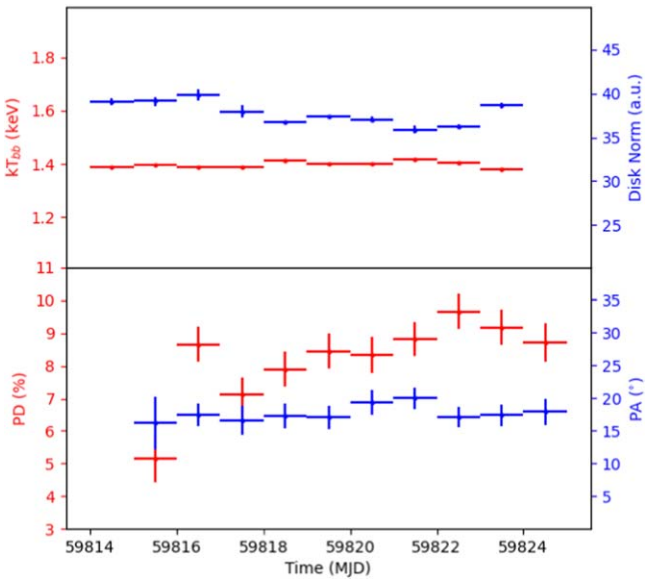


**Figure 4.** Top panel: time variability of the inner disk temperature ($kT_{\rm bb}$; red) and the BB normalization (blue). Bottom panel: time variability of the PD (red) and PA (blue). The error bars are shown at 68% confidence levels.

## 3. Theoretical Modeling of the Spectropolarimetric Results

Our polarimetric results for 4U 1630−47 are challenging to explain with existing models. Specifically, the PD is very high and increases with energy. In this section, we discuss progressively more complex models for the emergent PD that would be measured by an observer in the rest frame of the radiating plasma.

The PD measured by a distant stationary observer is additionally influenced by general relativistic (GR) effects. There are two main effects. First, as the polarization vector is parallel transported along null geodesics in a curved spacetime, the polarization direction projected onto the sky changes, so that the competing contributions coming from different parts of the disk partially cancel each other (Stark & Connors 1977; Dovčiak et al. 2008). Second, photons following the spacetime curvature can return to the disk and scatter off it. Since photons reflected upon the disk are expected to be polarized perpendicularly to those arriving directly to the observer (Schnittman & Krolik 2009; Taverna et al. 2020), the contributions of direct and returning radiation again partially cancel each other. Both of these effects thus reduce the overall PD from the rest-frame value, meaning that the models discussed in this section must be able to produce PD in the rest frame greater than what we observe for 4U 1630−47 to have a chance of reproducing the data once GR effects are included.

### 3.1. Analytical Results

We first consider the classical framework of pure electron scattering in a semi-infinite atmosphere (Chandrasekhar 1960;

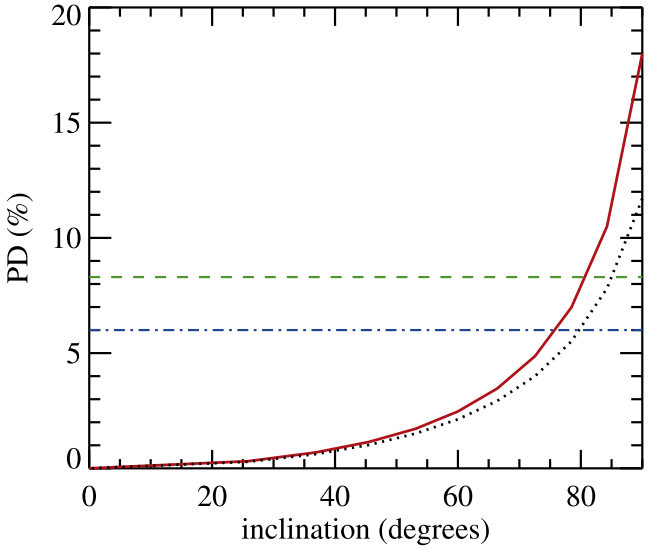


**Figure 5.** PD as a function of inclination for the pure electron-scattering atmosphere (black dotted line) compared to the case of partial ionization of matter (absorption effects) and distributed sources (red solid line). The blue dotted–dashed and green dashed lines show the most likely values of PD derived in the 2.0–2.6 and 2.0–8.0 keV bands, respectively.

Sobolev 1963). In this case, the PD is constant with energy since Thomson scattering is energy-independent. If the disk is flat and relativistic effects are absent, the PA is aligned with the disk plane and does not depend on energy. Figure 5 (black dashed line) shows how PD increases with observer inclination. We see that, even ignoring depolarizing GR effects, the 2–8 keV polarization of 4U 1630−47 (green dashed line) can only be reproduced for an inclination of $\sim 85^{\circ}$. At such high inclinations, the X-ray source becomes obscured by the outer parts of the accretion disk, for which an opening angle of $\sim 12^{\circ}$ has been observed (de Jong et al. 1996). Furthermore, complete eclipses are expected in this case but have not been detected in this source. Once GR effects are taken into account, the PD is below the observed 2–8 keV values even for an edge-on observer. Therefore, the classical pure electron-scattering atmosphere model fails to reproduce both the energy dependence and overall value of the observed PD.

Additionally, considering absorption opacity (i.e., relaxing the oversimplified assumption of complete ionization of matter in the disk atmosphere) can significantly enhance the PD of escaping spectra (Lightman & Shapiro 1975; Loskutov & Sobolev 1979). The red solid line in Figure 5 represents the calculation of Loskutov & Sobolev (1981; their Table 3, first column). Here, true absorption is included analytically by defining the ratio $\lambda$ of the scattering to the total, true absorption + scattering, coefficients and setting it to $\lambda = 0.5$. We see that the increase in PD over the pure electron-scattering case is greater for larger inclinations. This is because photons that already entered the disk atmosphere traveling approximately along the inclined observer's LOS before experiencing a scattering with a small scattering angle pass through a greater absorption optical depth on their way through the disk atmosphere and are therefore more likely to be absorbed than photons that entered the atmosphere vertically and experienced a scattering high in the atmosphere with a large scattering angle to emerge along the LOS. Absorption therefore increases the relative number of photons that reach the observer via a large scattering angle, thus increasing the PD. Here, the effect of photons being emitted in the atmosphere itself is included. This decreases the PD as compared to the classical Milne problem (Milne 1921), whereby all the photons originate from the bottom of the atmosphere, but we see that the PD is still higher than the pure electron-scattering atmosphere model. The emergent PD is now equal to the observed 2–8 keV PD at an inclination compatible with the maximum inclination expected for noneclipsing BHXRBs $i_{\max} \sim 78^{\circ}$ (de Jong et al. 1996).

However, the simple absorption model considered here cannot explain the observed PD with a reasonable inclination angle once depolarizing GR effects are taken into account. Moreover, if we wish to explain an energy dependence of PD, we must account for the energy dependence of the absorption coefficient in place of simply parameterizing the ratio of scattering to total opacity. We must therefore consider a more sophisticated treatment of the disk atmosphere.

### 3.2. Radiative Transfer Calculations of a Plane-parallel Disk Atmosphere Embedded in Flat Spacetime

We now include energy-dependent absorption in our model, accounting for the effects of partial ionization of different atomic species on the polarization properties within a passive plane-parallel slab on top of a source of unpolarized isotropic single-temperature BB radiation. This scenario resembles the Milne problem, but the ionization structure of the medium is precomputed, rather than parameterized. We derived the 1D vertical ionization profiles for different photoionization equilibrium (PIE) regimes using the `TITAN` (Dumont et al. 2003) and `CLOUDY` (Ferland et al. 2017) codes and for different collisional ionization equilibrium (CIE) regimes using the `CLOUDY` code only, as originally discussed by Taverna et al. (2021) and Podgorný et al. (2022). The ionization profile is subsequently used as input for the 3D Monte Carlo radiative transfer code `STOKES` (Goosmann & Gaskell 2007; Marin et al. 2012, 2015; Marin 2018). We find that the change of the emergent radiation PD with energy strongly depends on the ionization profile itself, rather than on the physical conditions (i.e., either PIE or CIE) that led to a certain ionization profile. We therefore present only results assuming PIE, following Taverna et al. (2021) and Podgorný et al. (2022). As the ionization profiles from both codes in PIE agree with each other, we limit the following discussion to the results obtained with the `TITAN` code precomputations used in `STOKES`. We adopt the typical solar abundance from Asplund et al. (2005), with $A_{\rm Fe} = 1.0$, which is important for the energy-dependent contribution of ionization edges. We present calculations that assume a constant density throughout the atmosphere. We neglect Compton upscattering, since it would be effective for higher slab temperatures than those considered in our modeling, and the effects would be visible only at energies above IXPE band. On the other hand, multiple Compton downscatterings are included, and this process is important in the genesis of polarization within the IXPE band.

Figure 6 shows the PD of the emergent radiation as a function of energy for different slab optical depths $\tau$, observer's inclinations $i$, and temperatures $kT_{\rm BB}$ of the illuminating BB for a highly ionized slab (density $n({\rm H}) = 10^{18}\,{\rm cm}^{-3}$). The optical depth is changed only by changing the height of the layer, ensuring that different optical depths in the plot correspond to the same density and ionization structure. In this respect, increasing the optical depth and inclination show similar effects (both enhancing PD), as photons are on average reaching the

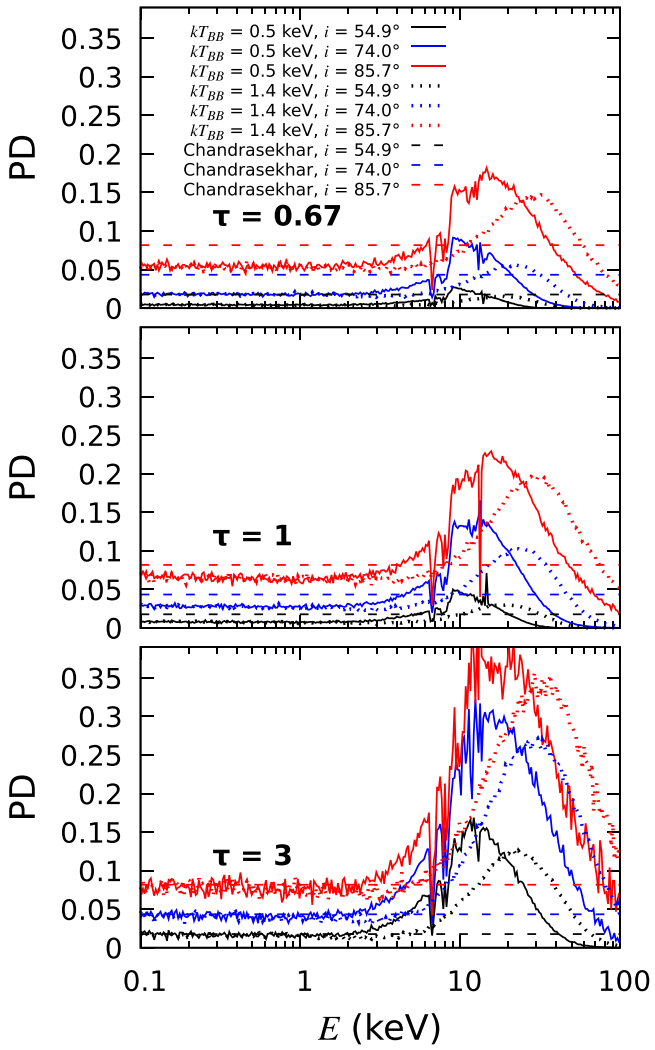


**Figure 6.** PD vs. energy from the TITAN and STOKES codes for a highly ionized slab ($n(\mathrm{H}) = 10^{18}$ cm$^{-3}$ and a standard BB normalization of the flux at the bottom of the slab). The observer's inclination and optical depth of the slab scale PD according to the energy-dependent contribution of both absorption and scattering. The BB temperature of the incident radiation sets weights on different energies. The Chandrasekhar scattering limit is reached for $\tau \geqslant 3$ at energies of $\leqslant 2$ keV for all significantly contributing single-color BBs. The obtained PA in all the studied cases is constant with energy and oriented to be parallel to the slab.

observer through larger portions of the slab. We see that the PD increases with energy in the 2–8 keV range, as is observed for 4U 1630−47. The energy dependence is a result of trade-offs between the relative importance of absorption and scattering and is thus highly dependent on the ionization parameter. Absorption boosts the PD, and so energy ranges where the absorption cross section is larger exhibit a higher PD than the pure scattering limit. From a wider X-ray energy perspective, the cross section for photoelectric absorption declines as $\sim E^{-3}$, while the scattering cross section remains roughly constant until $\approx$50 keV and should dominate over absorption already above $\approx$0.2 keV. However, in the IXPE band, this general trend is reversed; around 2 keV, the photoelectric absorption is insignificant, in accordance with the general trend, due to the lack of ionization edges, while at higher energies, the polarization properties are still strongly affected by absorption (depending on the BB temperature), mostly due to the highly ionized iron edge at $\sim$9 keV. We find that this iron edge is still important even for the highest ionization states achievable with the utilized radiative transfer codes under the studied conditions. We refer the reader to the detailed study by Davis et al. (2005; see their Figures 1 and 4), which estimates the energy-dependent contributions of various processes to the total opacity in the atmosphere of BHXRB disks. Compton down-scattering also contributes to PD increasing with energy, since photons that experience more scatterings have a lower energy and a lower PD.

For the moderate ionizations explored in Taverna et al. (2021), the PD instead *decreases* in the IXPE bandpass due to high absorption opacity at $\sim$2 keV (their Figure 3). This $\sim$2 keV opacity disappears for ionization parameters above $\xi = 4\pi F_{\mathrm{BB}}/n(\mathrm{H}) \gtrsim 10^5$ erg cm s$^{-1}$, leading to the trend that we see in Figure 6 with PD close to the pure scattering Chandrasekhar–Sobolev limit at $\sim$2 keV for $\tau \gtrsim 3$. The trend of rising PD with energy that we observe for 4U 1630−47 can therefore only be reproduced for a range of ionization states. The PA is constant with energy and parallel to the slab plane for all parameter combinations trialed. We find that the vertical stratification of the atmosphere in up to 50 plane-parallel layers gives the same results as a single layer, as long as the medium is highly ionized. Additional calculations show that vertically stratified atmospheres with BB temperatures down to $kT_{\mathrm{BB}} = 0.5$ keV, constant densities up to $n(\mathrm{H}) = 10^{20}$ cm$^{-3}$, and optical thicknesses $\tau \lesssim 10$ give approximately the same net 2–8 keV PD as the simplified approach. The model described above breaks for larger values of the optical depth, since (i) the required level of ionization on the distant (not illuminated) side of the passive slab in PIE is no longer reached, and (ii) the assumption of a passive slab is not valid due to the lack of internal sources of X-ray radiation inside the slab in our computations. The change in the emergent polarization due to the addition of internal sources is assessed in Appendix B for a semi-infinite atmosphere leading to the same estimates of locally emergent polarization at 2 keV for inner disk rings.

Thus, the observed 6% PD at 2 keV robustly constrains the inclination of the emitting patches to be equal to or exceed 80° (Figure 5). Figure 7 shows a fit of the output from these radiative transfer calculations to the IXPE data (i.e., ignoring GR effects), approximating the accretion disk with a plane-parallel slab in flat space. The best fits are achieved for optically thick slabs ($\tau \approx 5$) and high inclinations ($i \approx 84°$), depending on the temperature of the incident BB radiation. As relativistic effects tend to lower the PD, even higher local optical depths and/or inclinations are needed in the case of relativistic accretion disks.

### 3.3. Outflowing Disk Atmosphere

To enhance the degree of local polarization in these models for achievable inclination angles, it would be necessary to hypothesize a greater emission angle in the local reference frame comoving with the accretion disk. This could occur in case of an outflow with relativistic speed in the vertical direction, i.e., perpendicular to the disk. A similar analogy to this could be the outflowing corona models at relativistic velocities proposed to explain the IXPE observations of Cygnus X-1 (Poutanen et al. 2023). Due to the relativistic aberration effect, the photons must be emitted with higher emission angles to reach the same observer at a given inclination angle. Thus, we assume a disk atmosphere with decreasing radial profile of the vertical outflow velocity, i.e.,

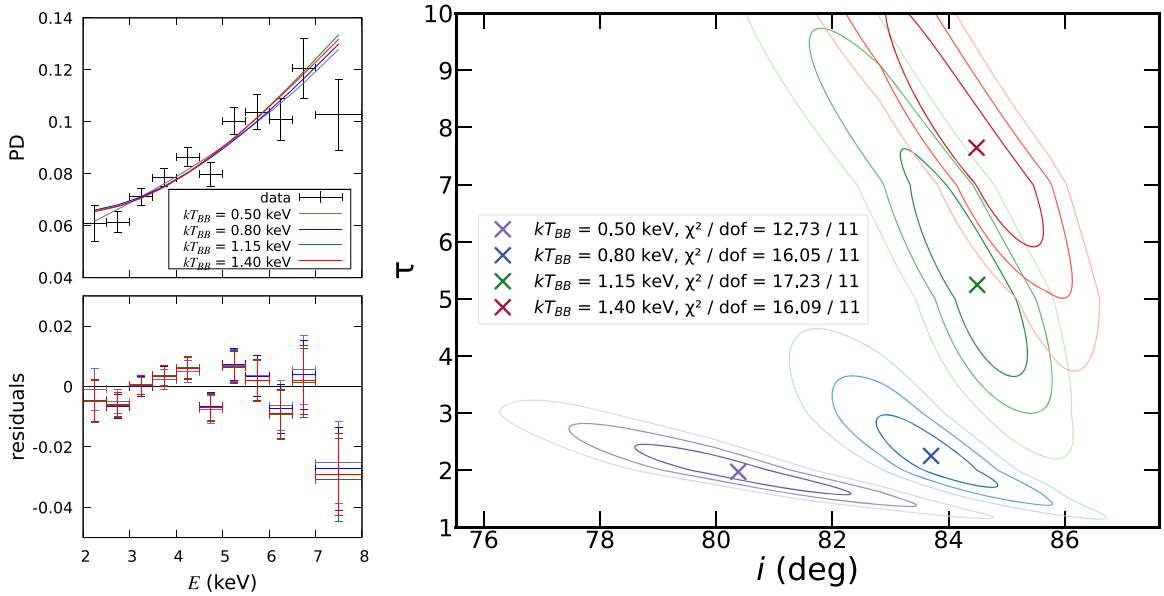


**Figure 7.** Best-fit local atmosphere solutions of PD vs. energy (left) and 2D contours at $1\sigma$, $2\sigma$, and $3\sigma$ levels around their value in the $i$–$\tau$ space (right) obtained with XSPEC by fitting the energy-dependent data with smoothed TITAN and STOKES models for $kT_{\rm BB} = 0.50$, 0.80, 1.15, and 1.40 keV.

$\beta(r) = \beta_0\, r^{-q}$, with $\beta$ being the speed in units of $c$ in the vacuum. This will add two additional parameters, $\beta_0$ and $q$, influencing the predicted polarization properties. The inclusion of this relativistic aberration to the two models and a comparison to the data are shown in the next section.

## 4. Comparison of Our Models with the Data

We now include all GR effects (see Appendix B for details) and compare our model predictions with the observed data. Since system properties such as inclination, distance, BH mass, and spin are not measured for this object but rather estimated indirectly, we study the polarization properties of our models assuming several values of high inclination and BH spin. Once the rest of the parameters that can change the spectral shape are derived from the fit of the observed spectrum, we fit the energy-dependent PD and PA, checking if any constraint can be put a posteriori on the spin and/or inclination. Since in this case we are interested in the thermal spectral component, and given that NuSTAR data only cover a small fraction of the IXPE observation (that we used to estimate the small contribution of the nonthermal component to the total flux), the spectral fits analyzed in this section refer to the NICER data set only. We emphasize that, excluding the nonthermal component, in the current analysis we use all the (summed) NICER data, i.e., not only the ones corresponding to the NuSTAR observations as in Section 2. Moreover, since the spectra observed by NICER are much better calibrated than those observed by IXPE (especially for high-flux sources), we use the IXPE data only for polarization.

We fit the NICER spectra using the model EDGE×TBABS×CLOUDY(KYNBBRR). Here, we use the Novikov–Thorne geometrically thin disk model KYNBBRR (Dovčiak et al. 2008; Taverna et al. 2020; Mikusincova et al. 2023, instead of and similar to the KERRBB model) for the thermal component, since this model allows us to also study the polarization properties in different scenarios. The other model components are the same as already described in Section 2. In the current spectral analysis, we use a 1% systematic error for the NICER data. Note that the spectral fit does not require the Comptonized component at these energies, confirming that its average contribution is very low in the full IXPE observation. The best spectral fits are summarized in Table E1.

In the next step, we froze all the spectral parameters that influence the spectral shape and tried to fit the observed PD and PA. To this purpose, we have developed different flavors of the KYNBBRR polarization model that originally assumed a Chandrasekhar approximation of a pure scattering atmosphere for direct radiation and a Chandrasekhar multiscattering approximation for polarization of reflected disk self-irradiation with an assumed albedo of 0.5. We denote this original model as model (A). The orientation of the system on the sky of the observer is the only free parameter of this model to fit the observed polarization properties. It defines the direction of the system rotation axis. Figure 8 (left panel) shows the results of fitting model (A) to the observed energy-dependent PD (parameters in Table E2). We see that (as mentioned in Section 3) the PD predicted by this model is too low (see the left panel of Figure 8 and Table E2).

To increase the local PD, we enhance model (A) by assuming a vertical outflow with relativistic speed as we described in detail in Section 3.3. The predicted polarization properties of this model, denoted as (B), are shown in Figure D1 and Table E2. This model still does not fit the observed polarization in a satisfactory way, failing to reproduce the PD increase with energy.

The third flavor of the polarization model, denoted as (C), uses the local PD derived by the model described in Section 3.2, i.e., an ionized passive slab with finite optical depth and constant density computed with the TITAN and STOKES codes. The local PD in this model depends on the disk temperature (given by the Novikov–Thorne temperature profile), emission angle (computed through a ray-tracing technique in the curved spacetime for a given observer inclination), and optical thickness of this layer. The latter is a new parameter that influences the predicted polarization properties. As mentioned in the previous sections, this model also does not fit the observed polarization properties (see the right panel of Figure D1 and Table E2): although the increase of PD with energy corresponds to what is observed, the PD magnitude is too low. In order to fix this issue, we increased the local PD by

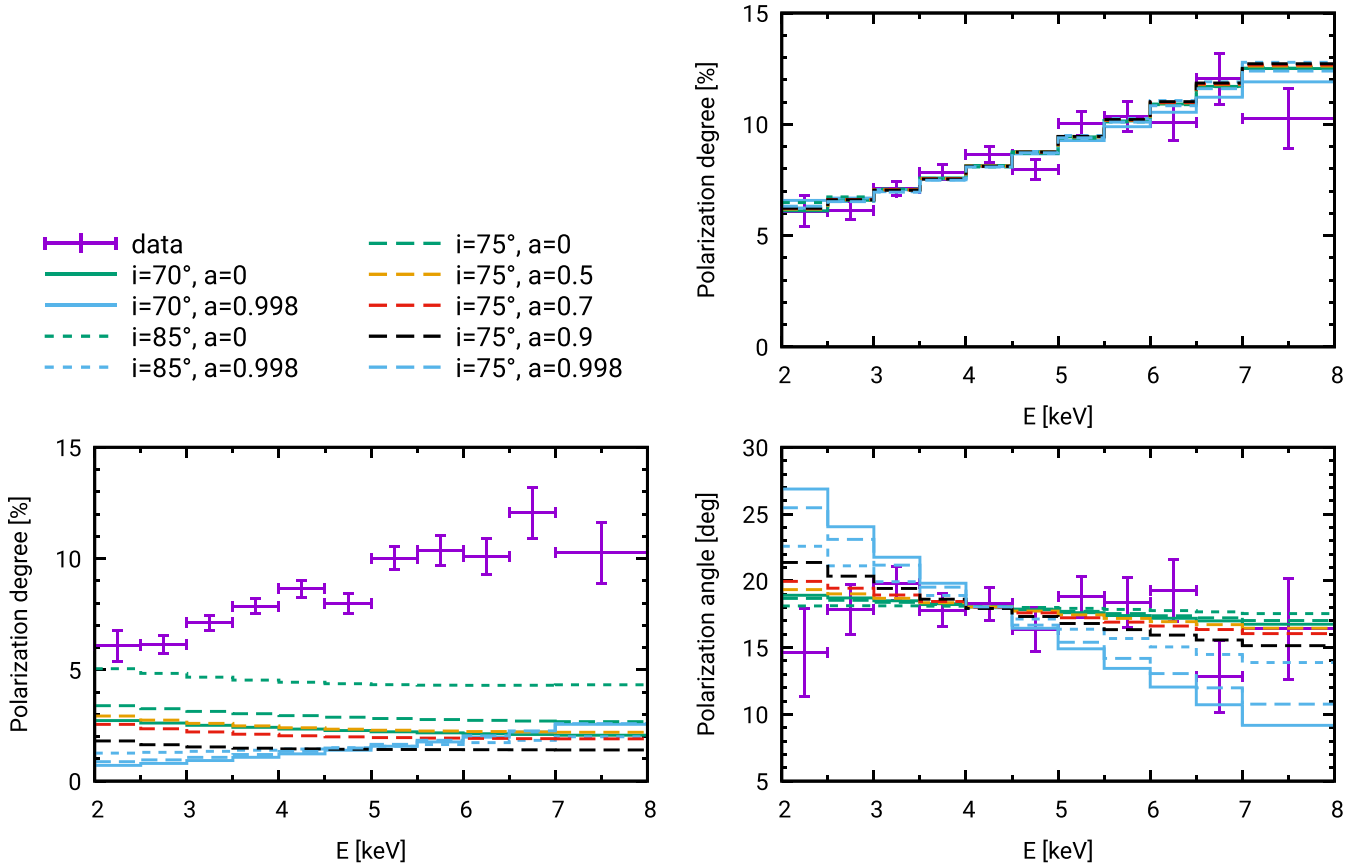


**Figure 8.** Comparison of the observed (purple points with error bars at 68% confidence level) and modeled 4U 1630–47 polarization properties (different lines). The standard Novikov–Thorne geometrically thin accretion disk model, with emission and reflection according to Chandrasekhar's pure scattering atmosphere model, significantly underpredicts the PD (left). The results of thin disk models with an outflowing, partially ionized atmosphere can explain the data for low and intermediate spins ($a = 0$, 0.5, or 0.7) and $i = 70°$ or 75° inclinations (top right and bottom right panels). The models shown in the right panels assume optical thickness $\tau = 7$ and an outflow velocity $v \sim 0.5c$.

assuming a vertical outflow velocity that causes a higher local emission angle due to aberration effects, as in model (B); we denote this as model (D). The top right panel of Figure 8 and Table E2 show that this model can fit the observed data quite well, except for highly spinning BHs, for which the fit of the observed PA is not satisfactory (see bottom right panel of Figure D2). Note that the PA energy dependence predicted with different flavors of the KYNBBRR model is very similar due to the fact that the local PA is always assumed to be parallel with the disk. The predicted PA is thus dependent mainly on the relativistic effects. Acceptable fits are denoted in bold in Table E2, and the best-fit parameters are shown in Table E3. Note that, in order to reproduce the observed PD, the scattering layer has to be outflowing with approximately half of the speed of light.

## 5. Discussion and Conclusions

The high PD and the energy dependence of the PD of 4U 1630–47 cannot be explained in the framework of the standard thin disk model, where the polarization of the thermal disk emission should roughly follow Chandrasekhar's classical result for a semi-infinite, free electron scattering atmosphere (Chandrasekhar 1960). Instead, radiative transfer calculations of a plane-parallel, partially ionized slab in PIE (Taverna et al. 2021; Podgorný et al. 2022), extensively discussed in Section 3.2, can predict a PD in the disk rest frame increasing from ∼6% at 2 keV to ∼10% at 8 keV (as observed), as long as the slab is highly ionized and viewed from an angle of ∼84°. The former condition is met for $kT_{\rm BB} \gtrsim 0.5$ keV, low ($\lesssim$10) optical depths, and a wide range of slab hydrogen densities, $n({\rm H}) \sim 10^{12}$–$10^{20}$ cm$^{-3}$. In this scenario, the PA should be parallel with the disk, although this cannot be assessed as yet due to the lack of constraints on the orientation of the radio jet. However, GR effects reduce the predicted observed PD in the IXPE energy band to well below the observed values (Figure E2 and Figure D1, right panel).

Additional corrections must be considered alongside those already discussed. We thus further assume particle outflows with relativistic vertical motion from the atmosphere of the disk. Due to relativistic beaming effects, this model will predict a higher PD. Including this in the partially ionized slab model, we can explain the observed PD and PA (right panels of Figure 8) with the combination of a low or intermediate BH spin ($a \lesssim 0.7$) and a highly ionized atmosphere with an optical depth of $\tau \sim 7$ outflowing perpendicular to the accretion disk at a velocity $v \sim 0.5c$. Note that a passive disk atmosphere is considered here with no internal sources of radiation, although the disk is quite hot. In Appendix B, we consider internal sources of radiation within the semi-infinite disk atmosphere in a different model but without any outflowing velocities, which also provides a too-low PD to explain the observed values. More detailed modeling is deferred to a future work.

The observed PD variability (see Figure 4) could then be explained by changes in the optical depth or due to varying outflow velocity of such an atmosphere. Consequently, the optical depth and the outflow velocity are anticorrelated.

Essentially, an increase in optical depth is analogous to a high inclination angle, just as increasing the outflow velocity would be. Hence, inclination angle, optical depth, and outflow velocity are all anticorrelated with each other.

The absorption lines imprinted on the spectrum with blueshift velocity $v \sim 0.003c$ originate from an equatorial wind located farther from the inner disk than the rapidly outflowing atmosphere. Previous analysis of the absorption lines using various instruments has indicated that absorption lines (especially Fe XXV and Fe XXVI) are found at a distance of $10^3$–$10^4$ gravitational radii ($R_g$) and with a mass outflow rate of 40% of the accretion rate (Díaz Trigo et al. 2014; King et al. 2014; Miller et al. 2015). Later, Fukumura et al. (2021) modeled these lines using a magneto-hydrodynamic (MHD) model, which starts at ISCO and is launched across the disk domain. Within that model, the inner regions of the outflow exhibit high relativistic velocities, which gradually decrease as a function of radial distances ($V \propto r^{-0.5}$). The matter is highly ionized close to the BH, and the absorption lines are found at a radius of $10^5 R_g$, where the ionization drops. Moreover, the velocity observed in the absorption lines represents the velocity along the LOS. However, the outflow may possess a higher-velocity component perpendicular to the accretion disk, consequently resulting in a smaller velocity into high inclination angles, as in the case of this source. It is plausible that the highly ionized and outflowing disk atmosphere could be connected to the absorption lines found at larger distances; i.e., the outflow is initially rapid and dense at the disk surface before spreading and slowing down at large distances like in the case of MHD winds (Blandford & Payne 1982; Contopoulos 1994; Ferreira 1997; Fukumura et al. 2010; Chakravorty et al. 2016). In a very approximate estimation, assuming an outflow with a vertical velocity (perpendicular to the disk plane) of $0.5c$ (as in the case of the outflowing disk atmosphere) at a distance of $1R_g$, it should result in an LOS velocity of $0.13c$ at an inclination angle of 75°. If we assume a radial dependence of $V \propto r^{-0.5}$ as in MHD models, this velocity will decrease to $0.004c$ at a distance of $10^3$ $R_g$, consistent with the velocity of the outer outflow found in this source. However, there has been no observational evidence indicating a connection between the inner and outer outflows. Conducting additional observations at varying continuum and line flux levels during different states would be necessary to investigate potential correlations between them.

Another possible way to explain the high polarization and its energy dependence would be increasing the contribution of the polarized flux through reflection due to disk self-irradiation. The underlying principle here is that the harder X-rays coming closer to the BH would have a higher fraction of photons returning back to the disk and getting reflected and hence higher polarization. Since this is dependent on the amount of self-irradiation, this can be larger only if we change the disk geometry, specifically if the disk scale height is substantially larger than in the geometrically thin accretion disk (as seen as well in Appendix C). The modeling described in Appendix C shows that geometrically thicker disks, such as the slim disk (Abramowicz et al. 1988) or recently very popular puffy disks (Wielgus et al. 2022), can lead to a large PD, increasing with energy. However, for the considered disk geometries, even our most optimistic fine-tuning of the model parameters (BH spin, inclination of the observer, disk scale height) cannot fully reproduce the observed high PD. We cannot exclude here that the high PD may be explained with other disk geometries that can increase the fraction of scattered X-rays even more.

To provide a rough estimate of the required increase in self-irradiation, we can use the geometrically thin disk scenario, where the albedo will be phenomenologically allowed to be larger than 1. The results of this experiment are shown in Figure 9. While the exact shape of the model-predicted PD and PA and thus also the dependence of the fit statistics on model parameters should be taken with caution, since the model is not self-consistent anymore, we can still discuss the value of the albedo and its interpretation with respect to the amount of self-irradiation. The required excess in albedo is the lowest for the highest studied spin value and increases for lower spin values, while it depends much less on the inclination. This is due to the fact that the amount of self-irradiation is already much larger in case of the disk reaching closer to the BH horizon for a highly spinning BH; thus, a smaller multiplicative factor (albedo) is needed to reach the needed increase in polarized reflected flux. On the other hand, the amount of the reflected self-irradiation depends much less on the inclination. For the inclination of 75°, the fitted albedo value was 4.5, 11.4, 17.1, 22.2, and 36.2 for the spin values of 0.998, 0.9, 0.7, 0.5, and 0, respectively. In the case of highly ionized accretion disks, the albedo is expected to be in the range of 0.5–1. Hence, a flux increase of the reflected self-irradiaton by a factor of at least 5–10 (in the case of a very highly spinning BH) with respect to the highly ionized geometrically thin disk would be required to explain the observed polarization. On the other hand, partial obscuration of the inner disk by the disk itself (self-shadowing) would decrease the contribution of the direct emission and in this way increase the relative contribution of the reflected self-irradiation component.

The high inclination could also be explained by a scenario where the inner accretion flow is more inclined than the binary system, like in the case of a wrapped disk. If the BH spin axis is not aligned with the binary orbital axis, the gravitational effects can result in the inner accretion flow becoming perpendicular to the BH spin axis, potentially leading to a greater inclination of the inner disk (Bardeen & Petterson 1975).

Our spectral analyses yielded a notably unphysical photon index, particularly in the third NuSTAR observation. Nevertheless, some studies have proposed a nonthermal/hybrid Comptonization model to explain the power-law tail observed in the soft state of BHBs, with a substantial contribution from the Comptonization from the nonthermal electron distribution (Gierliński et al. 1999; Zdziarski et al. 2001). Although the photon index values from our spectral analysis are phenomenological, they serve well our aim to understand the contribution from a power law in the IXPE energy band of 2–8 keV. Since the basic parameters of this system are not well known, especially the orientation of the system, it is difficult to understand the location of the corona. In case of the hard state of the BHB Cyg X-1, the PA aligned with the jet indicated that the corona was extended over the disk (Krawczynski et al. 2022). However, the geometry and location of the corona in the soft state are not understood well. Another observation of this source in the steep power-law (SPL) state dominated by the Comptonization component indicates that the Comptonization component is polarized in the same direction (perpendicular to the symmetric axis) and hence can be vertically extended along the symmetric axis of the system (Rodriguez Cavero et al. 2023). Indeed, the disk atmosphere can transition to a state dominated by inverse Compton scattering as the electrons gain energy, which can account for this behavior (Rodriguez Cavero et al. 2023). We refer the reader to the following paper on the SPL state of the source for a discussion on the geometry of the corona (Rodriguez Cavero et al. 2023).

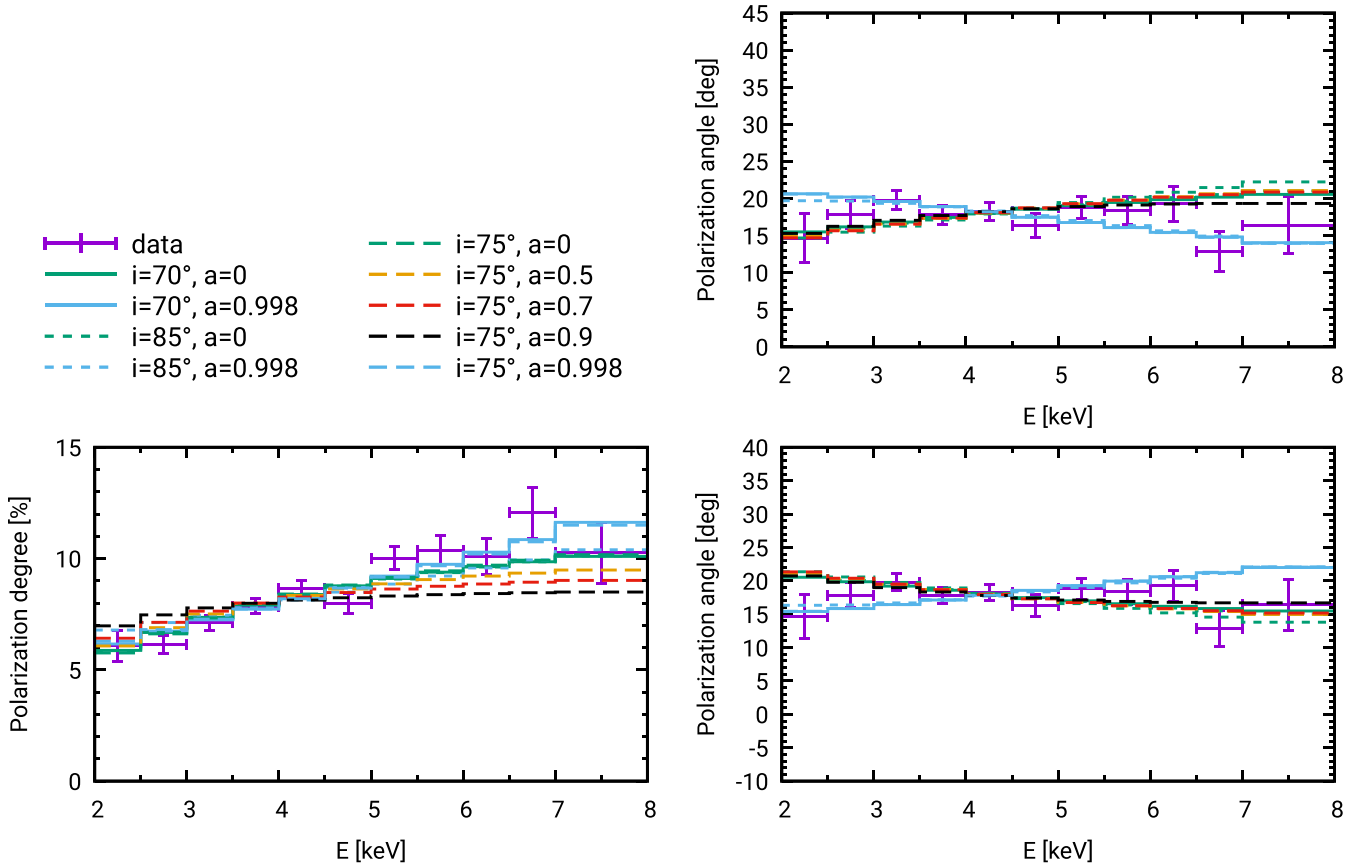


**Figure 9.** Energy-dependent PD (left) and PA for system rotation counterclockwise (top right) and clockwise (bottom right) in the case of a geometrically thin disk with the contribution of the reflected self-irradiation, increased by allowing the albedo to be larger than 1.

Two other works have independently analyzed the same IXPE data sets (Kushwaha et al. 2023; Rawat et al. 2023), obtaining observational results consistent with those presented in this work. The authors posit that the high PD can be explained by scattering off a wind. However, reflection off a highly ionized wind via Thomson scatterings leads to rather constant PDs (Ratheesh et al. 2021; Veledina et al. 2023b), contrary to what is observed. Further, for the reflected flux to make a significant contribution to the total spectrum, the solid angle subtended by the wind to the X-ray source needs to be large; in this case, emission lines should be present, which we do not see in the NICER and NuSTAR energy spectra. Recently, Tomaru et al. (2024) studied a possible wind contribution to the polarization and concluded that the wind cannot explain the very high PDs observed in this source. Finally, in a subsequent observation of the source, when it exhibited an SPL state and no evidence for a wind was apparent, the PD and its energy dependence were similar to the high-soft state (Rodriguez Cavero et al. 2023), again arguing against a wind origin for the polarization. Additionally, we also confirm the negligible contribution of the Comptonized power law in the 2–8 keV band using broad energy-band data of NuSTAR.

We conclude that the new observational diagnostics provided by IXPE imply significant deviations from the standard thin disk model. Additional observations of the source in the same emission state at different flux levels and in different emission states will constrain the accretion disk geometry and properties even further.

## Acknowledgments

We thank the anonymous reviewer for the suggestions in improving this manuscript. The Imaging X-ray Polarimetry Explorer (IXPE) is a joint US and Italian mission. The US contribution is supported by the National Aeronautics and Space Administration (NASA) and led and managed by its Marshall Space Flight Center (MSFC), with industry partner Ball Aerospace (contract NNM15AA18C). The Italian contribution is supported by the Italian Space Agency (Agenzia Spaziale Italiana, ASI) through contract ASI-OHBI-2022-13-I.0, agreements ASI-INAF-2022-19-HH.0 and ASI-INFN-2017.13-H0, and its Space Science Data Center (SSDC) with agreements ASI-INAF-2022-14-HH.0 and ASI-INFN 2021-43-HH.0, and by the Istituto Nazionale di Astrofisica (INAF) and the Istituto Nazionale di Fisica Nucleare (INFN) in Italy. This research used data products provided by the IXPE Team (MSFC, SSDC, INAF, and INFN) and distributed with additional software tools by the High-Energy Astrophysics Science Archive Research Center (HEASARC) at NASA Goddard Space Flight Center (GSFC).

A.R. and F.T. thank Prof. Keigo Fukumura for useful discussions. M.D., J.Pod., J.S., and V.K. acknowledge the support from the Czech Science Foundation project GACR 21-06825X and the institutional support from the Astronomical Institute of the Czech Academy of Sciences RVO:67985815. J. Podgorný and V.K. thank the Czech-Polish mobility program (MŠMT 8J20PL037 and PPN/BCZ/2019/1/00069) and the European Space Agency PRODEX project 4000132152. M.D. and J. Podgorný especially thank Prof. Agata Różańska for

explanations and guidance using the TITAN code. H.K., N.R.C., and A.W. acknowledge NASA support through grants NNX16AC42G, 80NSSC20K0329, 80NSSC20K0540, NAS8-03060, 80NSSC21K1817, 80NSSC22K1291, and 80NSSC 22K1883 as well as support from the McDonnell Center for the Space Sciences. A.V., J.Pou., V.L., and S.S.T. acknowledge support from Academy of Finland grants 349144 and 355672. V. F.S. acknowledges Deutsche Forschungsgemeinschaft (DFG) support through grant WE 1312/59-1 and the German Academic Exchange Service (DAAD) support through project 57525212. A.I. acknowledges support from the Royal Society. The French collaborators acknowledge financial support from the French High Energy national program from CNRS and from the French Space Agency (CNES). M.N. acknowledges the support by NASA under award No. 80GSFC21M0002.

## Data Availability

Data availability: the IXPE, NICER, and NuSTAR data used in this analysis are from the HEASARC data archive. Code availability: the codes used to reduce and analyze the data are readily accessible on the HEASOFT web page (https://heasarc.gsfc.nasa.gov/docs/software/lheasoft/download.html) and within the *ixpeobssim* repository (https://ixpeobssim.readthedocs.io/en/latest/?badge=latest.494). Kindly address any correspondence and requests concerning the remaining codes to ajay.ratheesh@inaf.it.

## Appendix A
## Data Sets and Data Reduction

### A.1. IXPE

The IXPE consists of three independent telescopes, each made up of a mirror module assembly and a detector unit (DU; Ramsey et al. 2019; Baldini et al. 2021; Soffitta et al. 2021; Weisskopf et al. 2022). IXPE observed 4U 1630–47 from 2022 August 23 23:14 to 2022 September 2 18:54 for a total effective exposure of approximately 463 ks. The analysis of the IXPE data is performed using the ixpeobssim software, version 28.4.0 (Baldini et al. 2022), which is based on level 2 processed data. For our analysis, we used the combined data sample collected by the three identical DUs, with appropriate rotation to align them with the same reference system in sky coordinates. We utilized the SAOImage DS9 software (Joye & Mandel 2003) for the source and background region selection process. The source region was chosen as a circular area with a radius of 1′.0, centered at the region of maximum intensity within the field of view, consistent with the source location. The background region was defined as a concentric annulus with an inner radius of 2′.5 and outer radius of 4′.3. The ixpeobssim routine xpselect was used to produce the source and background event files.

The PD and PA were computed using the xpbin routine of ixpeobssim using the flag --algorithm PCUBE. Version 11 of the IXPE response functions was used to process the data. This approach enabled the calculation of the polarization properties in a model-independent manner. The xpbin routine allows us to perform the background subtraction from source files; note that the source-emission leakage into the background region does not affect the final source polarization estimation significantly. Then we have generated the OGIP standard FITS files of PD and PA together with the unit response files with the flx2xsp tool from the HEASOFT package (Nasa High Energy Astrophysics Science Archive Research Center, HEASARC 2014) so that we can directly feed them to XSPEC (Arnaud 1996) in order to perform poslarimetric fits. The xpselect and xpbin routines were also used to generate event files for the analysis of variability over time.

### A.2. NICER

NICER uses 52 silicon drift detectors, each with a paired single-scattering concentrator optic and mutually aligned on the sky (Gendreau et al. 2016); it is sensitive in the 0.2–12 keV range, offering <100 ns time resolution, and has a peak effective area of $\sim$2000 cm$^2$. NICER carried out 11 observations of 4U 1630–47 during the IXPE campaign, from 2022 August 22 to 2022 September 1. A total of 64 good time intervals (GTIs) have been used for our science analysis, for an aggregate time of $\approx$27 ks and a total of >11 million X-ray counts.

NICER data were reduced and processed with version 9 of the data analysis software NICERDAS. Data were filtered following standard practices but allowing data from SAA passages. For each GTI, data from detectors 14, 34, and 54 were excised owing to calibration problems among these subsets. Additionally, the average rates of overshoot, undershoot, and X-ray events per GTI were assessed, and any detector with >15 median absolute deviation was excluded for that GTI. All the exposure times were corrected for the detector dead time (<1%). The background spectra were computed using the 3C 50 background model (Remillard et al. 2022). Only GTIs of length $t > 60$ s and for which the background rate was 100 times below the source rate were used for the analysis. A total of 27 ks of simultaneous NICER observations were finally available for the analysis. The spectral and light-curve files were extracted from the event files using XSELECT version 2.5b, and the response files were generated using nicerarf and nicerrmf.

### A.3. NUSTAR

4U 1630–47 was observed three times by NuSTAR during the IXPE pointing (on 2022 August 25 and 29 and 2022 September 1) using the two coaligned X-ray telescopes, each one with a corresponding Focal Plane Module A (FPMA) and B (FPMB; Harrison et al. 2013). The total elapsed times of the three snapshots are 38.3, 31.6, and 32.5 ks, respectively. The level 1 data products were processed with the Data Analysis Software NuSTARDAS package (v. 2.1.2). Cleaned event files (level 2 data products) were produced and calibrated using standard filtering criteria with the nupipeline task and the NuSTAR calibration files 20220510, available in the CALDB database. Extraction radii for the source and background spectra were 60″. The spectra and light curves were then generated by the nuproducts routine of the NuSTARDAS package. FPMA and FPMB spectra were binned following the procedure described in Kaastra & Bleeker (2016) in order to have a signal-to-noise ratio greater than 3 in each spectral channel. The net observing times for the FPMA/FPMB data sets are 16.3/16.6, 13.2/13.4, and 14.8/15.0 ks for the three sets of NuSTAR data, respectively.

## Appendix B
## Modeling the Effects of the Impact of Radial Variations of the Properties of the Disk Atmosphere and Relativistic Effects

In this section, we calculate the polarization of the emission from accretion disks with realistic radially structured disk atmospheres accounting for relativistic effects (Suleimanov

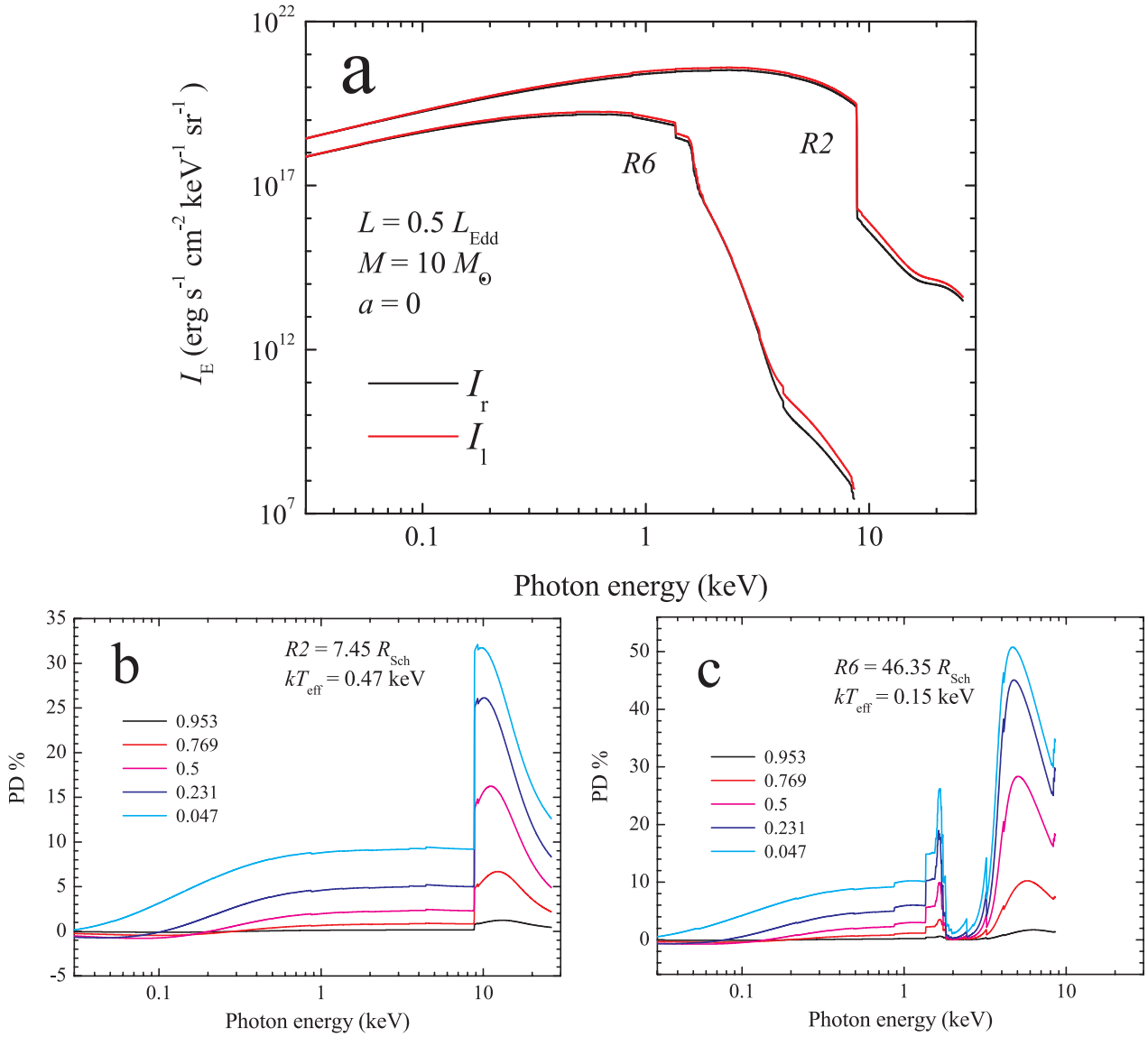


**Figure B1.** Spectra of two rings of the considered disk model (see text) in two modes (a) and PD for the same rings ((b) and (c)). The results in panels (b) and (c) are shown for five angles to the local normal; the cosines of the corresponding angles are reported in the panels.

et al. 2002, 2007). In these calculations, the radial disk structure follows from the conservation laws of mass, angular momentum, and energy in accordance with the standard Shakura–Sunyaev $\alpha$-disk model (Shakura & Sunyaev 1973) and the relativistic corrections by Novikov & Thorne (1973; see also Riffert & Herold 1995). The disk model was divided into a number of rings, and the vertical structure of each ring was calculated in the gray approximation using the model atmosphere approach (Suleymanov 1992). The model input parameters were taken from the disk parameters at a given radius: effective temperature, half-thickness, and surface density. The ring was assumed to be in hydrostatic and radiative equilibrium. It is also assumed that the local vertical energy release rate is proportional to the local pressure. Then we solve the radiation transfer equation in the 0.1–20 keV band (divided into 500 frequency points) using the gray ring model. We adopted the two-mode approximation, with electron scattering being the only source of polarization (see details in Suleimanov et al. 2023), and assumed no illumination from the top of the atmosphere, imposing a (mirror) reflection boundary condition in the midplane of the disk. The plasma equation of state is used assuming local thermodynamic equilibrium. We account for the 15 most abundant chemical elements assuming the solar chemical composition (Asplund et al. 2009); the ionization state of the elements and the excited level populations were computed using the Saha–Boltzmann equations, including pressure ionization effects (Hubeny et al. 1994). The absorption opacities were calculated accounting for bound–free and free–free transitions of all the elements. In Figure B1, we present the locally emitted energy spectra for two exemplary rings and five inclinations in the case of $M_{\rm bh} = 10\ M_{\odot}$, $L = 0.5 L_{\rm Edd}$, and $a = 0$. As expected, PD exhibits a maximum where the absorption opacity becomes comparable to the Thomson scattering one.

Exemplary results of the integrated disk spectra are shown in Figure B2, before and after accounting for relativistic effects. The detailed modeling confirms the results from the simpler models: the polarization predicted by the standard thin disk model is lower than the observed one.

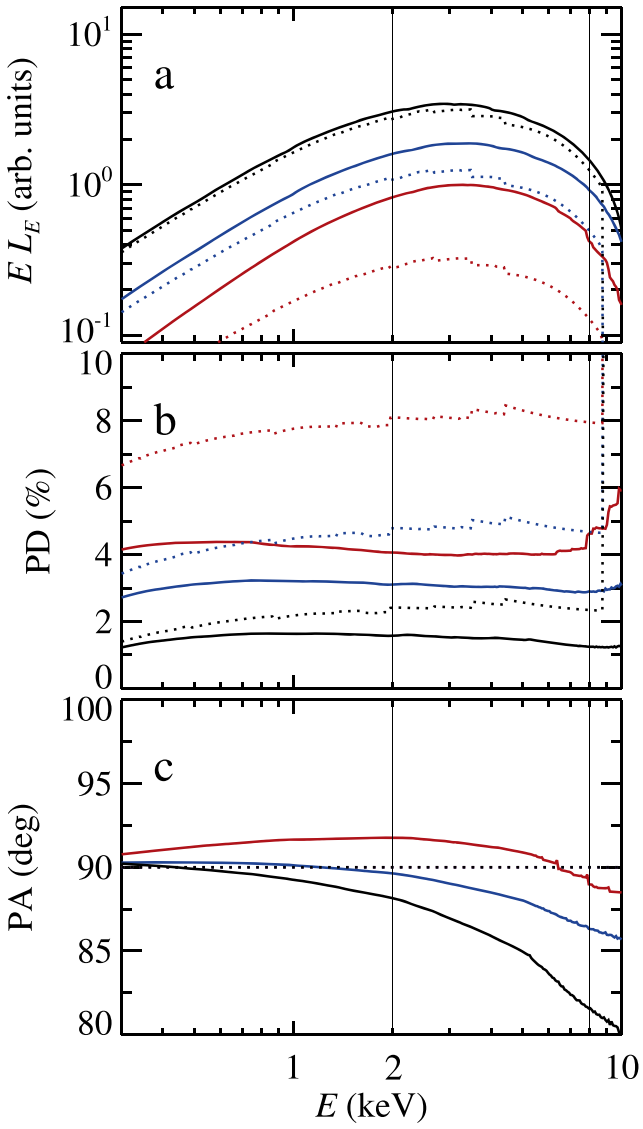


**Figure B2.** Spectra, PD, and PA from a self-consistent model of disk atmosphere in radial bins. Dotted and solid lines correspond to quantities in the local reference frame and modified by the relativistic effects (as seen by a distant observer), respectively. The results are shown for three disk inclinations: $i = 60°$ (black), 75° (blue), and 85° (red).

## Appendix C
## Polarization of the Emission from Slim and Thick Accretion Disks

Here we investigate phenomenological thick disk models (West & Krawczynski 2023) in order to check if the observed X-ray polarization properties can be explained in this scenario. The models assume disks of various scale heights embedded in the Kerr spacetime, with the disk matter orbiting the BH on GR Keplerian orbits. Following the classical treatment by Page & Thorne (1974), the disk material locally emits all the net energy that it gains by sinking toward the BH. Given the energy liberated in each radial bin per comoving time, the temperature of the disk surface is calculated from the Stefan–Boltzmann law, accounting for the fact that a thicker disk has a larger surface area than a geometrically thin disk. It is furthermore assumed that the disk locally emits a modified BB energy spectrum adopting a constant spectral hardening factor of 1.8. The surface of the disk follows a simple phenomenological description inspired by the Polish doughnut models by Abramowicz et al. (1988). The disks are characterized by the scale height $h/r$, with $h$ being the height of the disk where it is thickest and $r$ being the corresponding disk radius.

Figure C1 shows the 2D distribution of the surface brightness, PD, and PA as seen by a distant observer. Both plots show the effect of the colder and X-ray-dimmer outer portions of the slim disks shadowing the emission from the hot and bright inner regions. Figure C2 shows the PD and PA energy spectra for disk scale heights ranging between 0 and 0.9. The PD exhibits an increasing behavior across the IXPE band, as the highest-energy emission from the innermost portion of the disk is most likely to scatter off the opposite side of the disk. On the other hand, the PA stays roughly constant with energy, except for very low scale heights. Note that since the orientation of the system is unknown, we can check only the trend in energy behavior of PA, while its absolute value cannot be assessed. This is why we leave it unconstrained in Figure C2. The figure shows that increasing the scale height leads to overall higher values of the PD. However, we could not find a parameter combination that achieves a PD as high as the observed ones.

Figure C3 shows that the PDs increase with inclination and BH spin. The dependence of the PD on inclination results from the combined effects of different emission angles of the

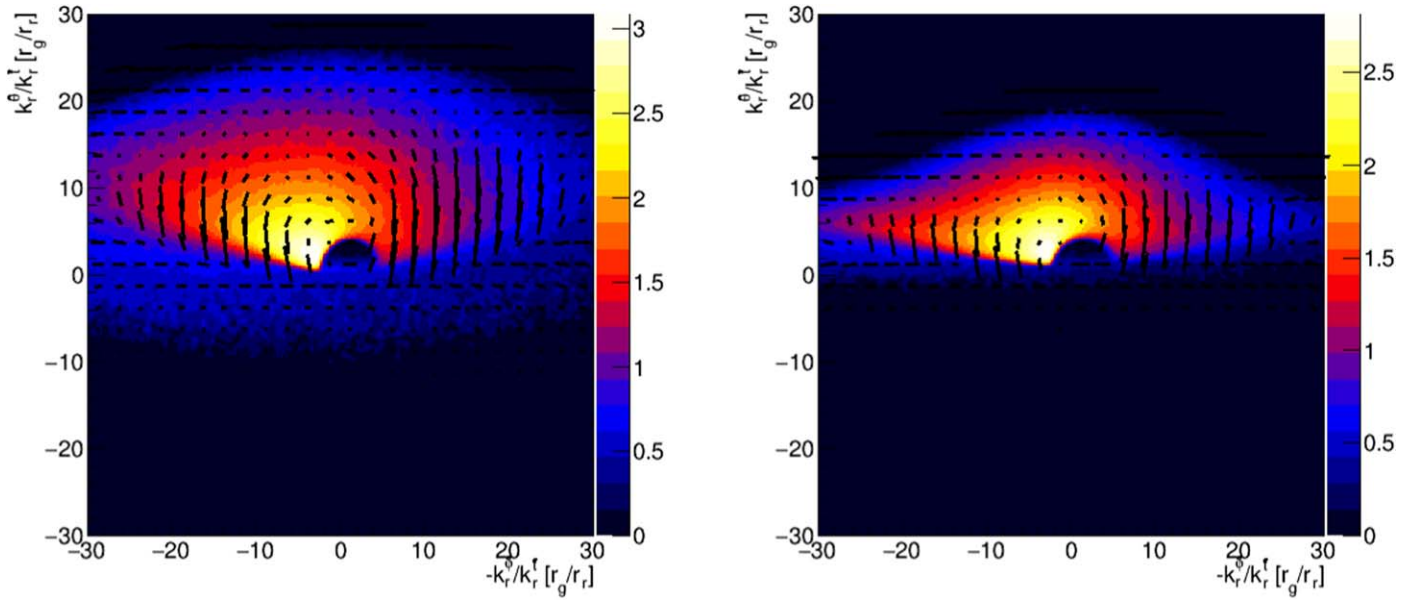


**Figure C1.** Total flux obtained from ray-traced simulations for a BH spin $a = 0.98$, with $h/r = 0.5$ viewed at a 75° inclination (left) and $h/r = 0.3$ viewed at an 85° inclination (right). The color scale shows the flux on a logarithmic scale in arbitrary units. Overlaid, the black vectors indicate the PA and have a length proportional to the PD, both as seen by a distant observer.

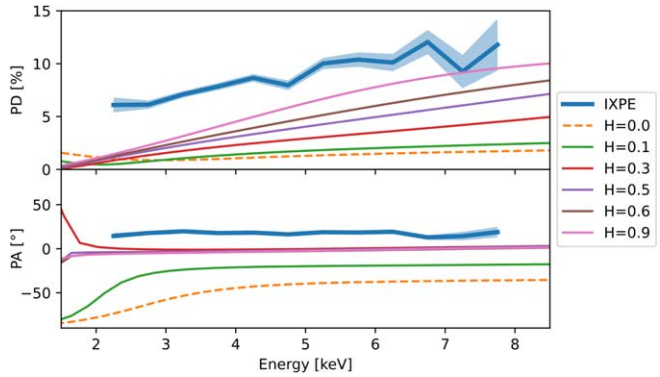


**Figure C2.** PD (top) and PA (bottom) for thin, slim, and thick disks for a BH spin of 0.98 viewed at $i = 85°$, assuming a highly ionized disk atmosphere. The model predictions are marked by solid lines of different colors (dashed lines correspond to the thin disk prediction), while IXPE data are reported as a blue line in both panels. The shaded cyan region represents the errors at the 68% confidence level.

photons reaching the observer and different degrees of self-shadowing of the emission by thick disks. Increasing the BH spin leads to higher PDs, as higher spins correspond to the disks extending closer to the BHs and leading to a higher fraction of photons reflecting off the disks.

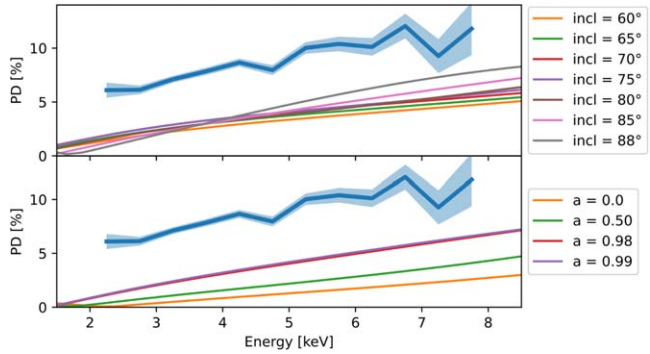


**Figure C3.** PD predictions for disks with scale height 0.5. Top panel: results for a BH with spin $a = 0.99$, viewed at different inclination angles. Bottom panel: results for a BH with different spins, viewed at an inclination of 85°.

## Appendix D
## Additional Figures

PD with respect to energy and the corresponding best fit for models B and C is given in Figure D1. Figure D2 shows the PA with respect to energy predicted by the best fit models for both clockwise and anti-clockwise direction.

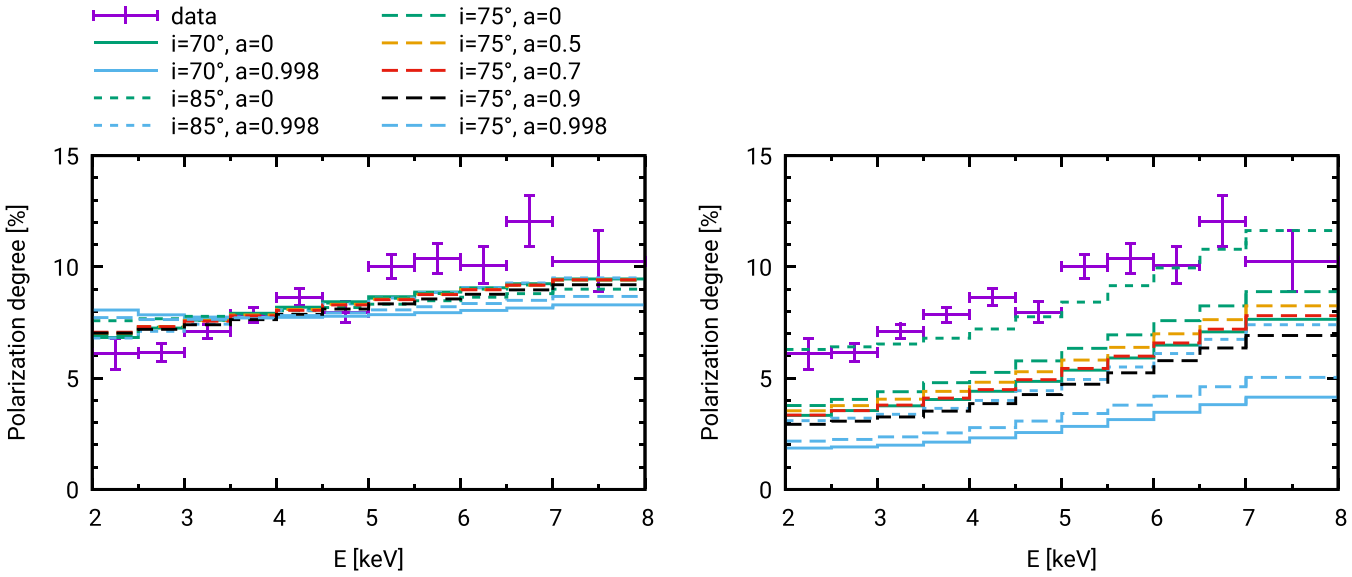


**Figure D1.** Attempted fits of the observed PD with models (B) (left) and (C) (right). We did not account for self-irradiation in these computations.

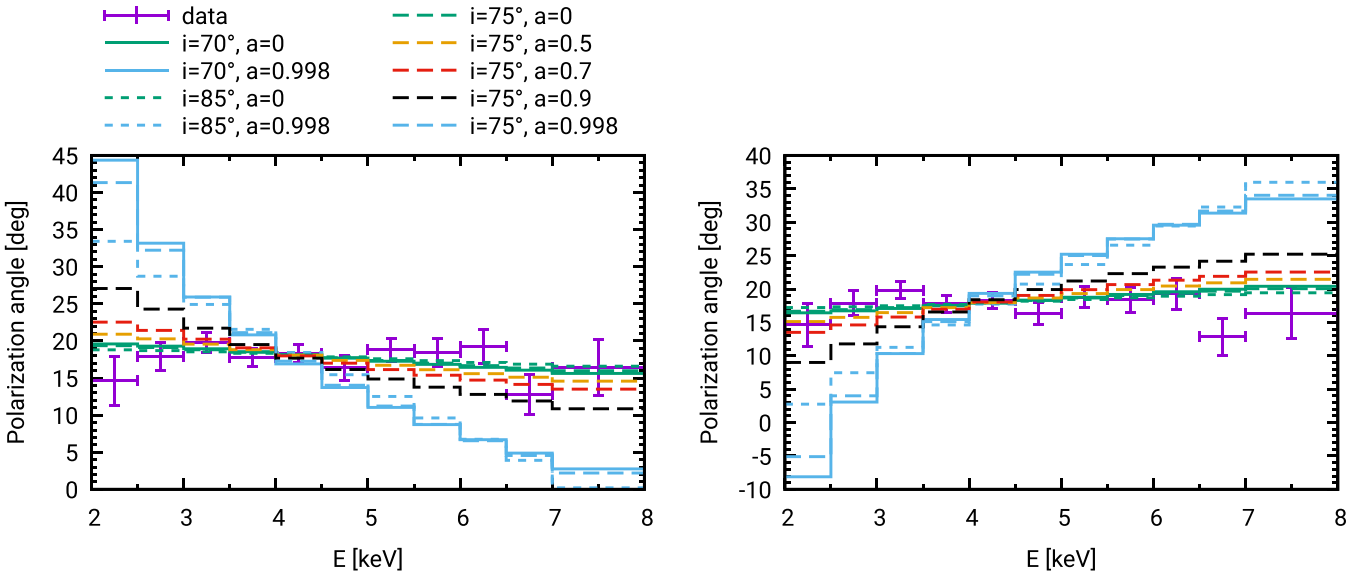


**Figure D2.** PA predicted by the models. The PA for both counterclockwise (left) and clockwise (right) directions of the system rotation are shown (the disk and BH are corotating in both cases).

## Appendix E
## Additional Tables

The best fit spectral parameters of the KYNBBRR model are summarised in Table E1. Comparison of the best fit for PD and PA for different flavors of the KYNBBRR model is shown in Table E2, while in Table E3, we show the best fit parameters of the KYNBBRR model with the relativistically outflowing ionized layer.

**Table E1**
Comparison of the Spectral Fit Results for Different Values of Inclination and BH Spin, with the KYNBBRR Model Representing the Thermal Component

| Incl. $i$ (deg) | Spin $a$ | Mass $M_{\rm bh}$ ($M_\odot$) | Accretion Rate $\dot{M}/\dot{M}_{\rm Edd}$ | Normalization norm | Fit Goodness $\chi^2$ (792 dof) |
|---|---|---|---|---|---|
| 70 | 0 | 3 (frozen) | $0.451 \pm 0.003$ | $2.13 \pm 0.02$[a] | 730 |
| | 0.998 | $23.59 \pm 0.10$ | $0.1221 \pm 0.0003$ | 0.75614 (frozen) | 638 |
| 75 | 0 | 3 (frozen) | $0.424 \pm 0.003$ | $3.02 \pm 0.03$[b] | 719 |
| | 0.5 | $3.59 \pm 0.02$ | $0.1992 \pm 0.0005$ | 4.93827 (frozen) | 732 |
| | 0.7 | $3.80 \pm 0.02$ | $0.1759 \pm 0.0005$ | 4.93827 (frozen) | 719 |
| | 0.9 | $15.57 \pm 0.07$ | $0.2402 \pm 0.0006$ | 0.75614 (frozen) | 670 |
| | 0.998 | $29.5 \pm 0.1$ | $0.1005 \pm 0.0002$ | 0.75614 (frozen) | 632 |
| 85 | 0 | 3 (frozen) | $0.6336 \pm 0.0005$ | 4.93827 (frozen) | 728 |
| | 0.998 | $48.7 \pm 0.2$ | $0.0724 \pm 0.0002$ | 0.75614 (frozen) | 629 |

**Notes.** If not noted otherwise, a source distance of 11.5 kpc is assumed, corresponding to a normalization of 0.76. In case the fitted BH mass hit the lower limit of 3 $M_\odot$, we assumed a distance of 4.5 kpc corresponding to a model normalization of 4.9. In case the fitted BH mass hit the lower limit of 3 $M_\odot$ again, we assumed 3 $M_\odot$ as the BH mass and fitted the normalization that corresponds to $\texttt{norm} = 1/D_{10}^2$, with $D_{10}$ being the distance to the source in units of 10 kpc. The fitted values of the TBABS and CLOUDY parameters were close to the values shown in Table 3.
[a] Corresponding to a distance of 6.85 kpc.
[b] Corresponding to a distance of 5.75 kpc.

**Table E2**
Comparison of PD and PA Fits Using Different Flavors of the KYNBBRR Model

| Incl. $i$ (deg) | Spin $a$ | Model (A) $\chi^2$(PD/PA/tot) | Model (B) $\chi^2$(PD/PA/tot) | Model (C) $\chi^2$(PD/PA/tot) | Model (D) $\chi^2$(PD/PA/tot) |
|---|---|---|---|---|---|
| 70 | 0 | 1573/8.9/1581 | 33/8.0/40 | 626/7.7/634 | **11.5/7.9/19.4** |
| | 0.998 | 2236/280/2517 | 84/80/164 | 1551/66/1617 | 12.2/57/69 |
| 75 | 0 | 1132/7.8/1140 | 35/7.8/43 | 387/7.7/395 | **11.8/7.8/19.6** |
| | 0.5 | 1529/13/1542 | 37/8.8/45 | 506/8.3/514 | **12.2/8.3/20.5** |
| | 0.7 | 1722/21/1743 | 37/10/47 | 606/9.8/616 | **12.5/9.3/21.8** |
| | 0.9 | 2077/53/2130 | 41/15/56 | 828/15/843 | 12.7/12.9/25.7 |
| | 0.998 | 2162/258/2420 | 65/56/121 | 1309/48/1357 | 12.1/41/53 |
| 85 | 0 | 658/7.8/666 | 55/7.7/63 | 42/7.9/50 | **13.3/7.9/21.2** |
| | 0.998 | 2098/187/2285 | 30/21/51 | 765/21/786 | 12.9/18.6/31.54 |

**Note.** Note that both PD and PA were binned in 11 energy bins. The fits with $\chi^2_{\rm tot} < 22$ are denoted in bold, and the best-fit parameter values of these cases are shown in Table E3.

**Table E3**
Best-fit Parameters of the KYNBBRR Model (D) with Outflowing Ionized Layer

| Incl. $i$ (deg) | Spin $a$ | Orientation $\chi_o$ | Speed Norm. $\beta_0$ | Speed Index $q$ | Speed $\beta(T_{\rm max})$ |
|---|---|---|---|---|---|
| 70 | 0 | $-70.7 \pm 0.5$ | $0.65 \pm 0.14$ | $0.54 \pm 0.19$ | 0.50 |
| 75 | 0 | $-71.2 \pm 0.5$ | $0.56 \pm 0.18$ | $0.72 \pm 0.29$ | 0.40 |
| | 0.5 | $-70.1 \pm 0.5$ | $0.65 \pm 0.18$ | $0.73 \pm 0.26$ | 0.47 |
| | 0.7 | $-68.9 \pm 0.5$ | $0.71 \pm 0.17$ | $0.70 \pm 0.23$ | 0.53 |
| 85 | 0 | $-72.5 \pm 0.5$ | 0.6 (frozen) | $2.1 \pm 0.2$ | 0.22 |

**Note.** Since the optical thickness of the layer and its outflow speed were degenerate and are anticorrelated, we eventually froze the optical thickness at $\tau = 7$. The outflow speed (last column) is characterized by its value at the radius where the disk temperature peaks, $\beta(T_{\rm max})$.

## ORCID iDs

Ajay Ratheesh https://orcid.org/0000-0003-0411-4243
Michal Dovčiak https://orcid.org/0000-0003-0079-1239
Henric Krawczynski https://orcid.org/0000-0002-1084-6507
Jakub Podgorný https://orcid.org/0000-0001-5418-291X
Lorenzo Marra https://orcid.org/0009-0001-4644-194X
Alexandra Veledina https://orcid.org/0000-0002-5767-7253
Valery F. Suleimanov https://orcid.org/0000-0003-3733-7267
Nicole Rodriguez Cavero https://orcid.org/0000-0001-5256-0278
James F. Steiner https://orcid.org/0000-0002-5872-6061
Jiří Svoboda https://orcid.org/0000-0003-2931-0742
Andrea Marinucci https://orcid.org/0000-0002-2055-4946
Stefano Bianchi https://orcid.org/0000-0002-4622-4240
Michela Negro https://orcid.org/0000-0002-6548-5622
Giorgio Matt https://orcid.org/0000-0002-2152-0916
Francesco Tombesi https://orcid.org/0000-0002-6562-8654
Juri Poutanen https://orcid.org/0000-0002-0983-0049
Adam Ingram https://orcid.org/0000-0002-5311-9078
Roberto Taverna https://orcid.org/0000-0002-1768-618X
Andrew West https://orcid.org/0000-0002-5471-4709
Vladimir Karas https://orcid.org/0000-0002-5760-0459
Francesco Ursini https://orcid.org/0000-0001-9442-7897
Paolo Soffitta https://orcid.org/0000-0002-7781-4104
Fiamma Capitanio https://orcid.org/0000-0002-6384-3027
Domenico Viscolo https://orcid.org/0000-0002-7076-9929
Alberto Manfreda https://orcid.org/0000-0002-0998-4953
Fabio Muleri https://orcid.org/0000-0003-3331-3794
Maxime Parra https://orcid.org/0009-0003-8610-853X
Banafsheh Beheshtipour https://orcid.org/0000-0002-8524-1537
Sohee Chun https://orcid.org/0009-0002-2488-5272
Nicolò Cibrario https://orcid.org/0000-0003-3842-4493
Niccolò Di Lalla https://orcid.org/0000-0002-7574-1298
Sergio Fabiani https://orcid.org/0000-0003-1533-0283
Kun Hu https://orcid.org/0000-0002-9705-7948
Philip Kaaret https://orcid.org/0000-0002-3638-0637
Vladislav Loktev https://orcid.org/0000-0001-6894-871X
Romana Mikušincová https://orcid.org/0000-0001-7374-843X
Tsunefumi Mizuno https://orcid.org/0000-0001-7263-0296
Nicola Omodei https://orcid.org/0000-0002-5448-7577
Pierre-Olivier Petrucci https://orcid.org/0000-0001-6061-3480
Simonetta Puccetti https://orcid.org/0000-0002-2734-7835
John Rankin https://orcid.org/0000-0002-9774-0560
Silvia Zane https://orcid.org/0000-0001-5326-880X
Iván Agudo https://orcid.org/0000-0002-3777-6182
Lucio A. Antonelli https://orcid.org/0000-0002-5037-9034
Matteo Bachetti https://orcid.org/0000-0002-4576-9337
Luca Baldini https://orcid.org/0000-0002-9785-7726
Wayne H. Baumgartner https://orcid.org/0000-0002-5106-0463
Ronaldo Bellazzini https://orcid.org/0000-0002-2469-7063
Stephen D. Bongiorno https://orcid.org/0000-0002-0901-2097
Raffaella Bonino https://orcid.org/0000-0002-4264-1215
Alessandro Brez https://orcid.org/0000-0002-9460-1821
Niccolò Bucciantini https://orcid.org/0000-0002-8848-1392
Simone Castellano https://orcid.org/0000-0003-1111-4292
Elisabetta Cavazzuti https://orcid.org/0000-0001-7150-9638
Chien-Ting Chen https://orcid.org/0000-0002-4945-5079
Stefano Ciprini https://orcid.org/0000-0002-0712-2479
Enrico Costa https://orcid.org/0000-0003-4925-8523
Alessandra De Rosa https://orcid.org/0000-0001-5668-6863
Ettore Del Monte https://orcid.org/0000-0002-3013-6334
Laura Di Gesu https://orcid.org/0000-0002-5614-5028
Alessandro Di Marco https://orcid.org/0000-0003-0331-3259
Immacolata Donnarumma https://orcid.org/0000-0002-4700-4549
Victor Doroshenko https://orcid.org/0000-0001-8162-1105
Steven R. Ehlert https://orcid.org/0000-0003-4420-2838
Teruaki Enoto https://orcid.org/0000-0003-1244-3100
Yuri Evangelista https://orcid.org/0000-0001-6096-6710
Riccardo Ferrazzoli https://orcid.org/0000-0003-1074-8605
Javier A. Garcia https://orcid.org/0000-0003-3828-2448
Shuichi Gunji https://orcid.org/0000-0002-5881-2445
Jeremy Heyl https://orcid.org/0000-0001-9739-367X
Wataru Iwakiri https://orcid.org/0000-0002-0207-9010
Svetlana G. Jorstad https://orcid.org/0000-0001-9522-5453
Fabian Kislat https://orcid.org/0000-0001-7477-0380
Jeffery J. Kolodziejczak https://orcid.org/0000-0002-0110-6136
Fabio La Monaca https://orcid.org/0000-0001-8916-4156
Luca Latronico https://orcid.org/0000-0002-0984-1856
Ioannis Liodakis https://orcid.org/0000-0001-9200-4006
Simone Maldera https://orcid.org/0000-0002-0698-4421
Frédéric Marin https://orcid.org/0000-0003-4952-0835
Alan P. Marscher https://orcid.org/0000-0001-7396-3332
Herman L. Marshall https://orcid.org/0000-0002-6492-1293
Francesco Massaro https://orcid.org/0000-0002-1704-9850
Stephen C.-Y. Ng https://orcid.org/0000-0002-5847-2612
Stephen L. O'Dell https://orcid.org/0000-0002-1868-8056
Chiara Oppedisano https://orcid.org/0000-0001-6194-4601
Alessandro Papitto https://orcid.org/0000-0001-6289-7413
George G. Pavlov https://orcid.org/0000-0002-7481-5259
Abel L. Peirson https://orcid.org/0000-0001-6292-1911
Matteo Perri https://orcid.org/0000-0003-3613-4409
Melissa Pesce-Rollins https://orcid.org/0000-0003-1790-8018
Maura Pilia https://orcid.org/0000-0001-7397-8091
Andrea Possenti https://orcid.org/0000-0001-5902-3731
Brian D. Ramsey https://orcid.org/0000-0003-1548-1524
Oliver J. Roberts https://orcid.org/0000-0002-7150-9061
Roger W. Romani https://orcid.org/0000-0001-6711-3286
Carmelo Sgrò https://orcid.org/0000-0001-5676-6214
Patrick Slane https://orcid.org/0000-0002-6986-6756
Gloria Spandre https://orcid.org/0000-0003-0802-3453
Douglas A. Swartz https://orcid.org/0000-0002-2954-4461
Toru Tamagawa https://orcid.org/0000-0002-8801-6263
Fabrizio Tavecchio https://orcid.org/0000-0003-0256-0995
Allyn F. Tennant https://orcid.org/0000-0002-9443-6774
Nicholas E. Thomas https://orcid.org/0000-0003-0411-4606
Alessio Trois https://orcid.org/0000-0002-3180-6002
Sergey S. Tsygankov https://orcid.org/0000-0002-9679-0793
Roberto Turolla https://orcid.org/0000-0003-3977-8760

Jacco Vink https://orcid.org/0000-0002-4708-4219
Martin C. Weisskopf https://orcid.org/0000-0002-5270-4240
Kinwah Wu https://orcid.org/0000-0002-7568-8765
Fei Xie https://orcid.org/0000-0002-0105-5826

## References

Abramowicz, M. A., Czerny, B., Lasota, J. P., & Szuszkiewicz, E. 1988, ApJ, 332, 646
Arnaud, K. A. 1996, in ASP Conf. Ser. 101, Astronomical Data Analysis Software and Systems V, ed. G. H. Jacoby & J. Barnes (San Francisco, CA: ASP), 17
Arzoumanian, Z., Gendreau, K. C., Baker, C. L., et al. 2014, Proc. SPIE, 9144, 914420
Asplund, M., Grevesse, N., Sauval, A. J., & Scott, P. 2009, ARA&A, 47, 481
Asplund, M., Grevesse, N., & Sauval, A. J. 2005, in ASP Conf. Ser. 336, Cosmic Abundances as Records of Stellar Evolution and Nucleosynthesis, ed. T. G. Barnes & F. N. Bash (San Francisco, CA: ASP), 25
Baldini, L., Barbanera, M., Bellazzini, R., et al. 2021, APh, 133, 102628
Baldini, L., Bucciantini, N., Lalla, N. D., et al. 2022, SoftX, 19, 101194
Bardeen, J. M., & Petterson, J. A. 1975, ApJL, 195, L65
Blandford, R. D., & Payne, D. G. 1982, MNRAS, 199, 883
Capitanio, F., Campana, R., De Cesare, G., & Ferrigno, C. 2015, MNRAS, 450, 3840
Chakravorty, S., Petrucci, P. O., Ferreira, J., et al. 2016, A&A, 589, A119
Chandrasekhar, S. 1960, Radiative transfer (New York: Dover)
Contopoulos, J. 1994, ApJ, 432, 508
Davis, S. W., Blaes, O. M., Hubeny, I., & Turner, N. J. 2005, ApJ, 621, 372
de Jong, J. A., van Paradijs, J., & Augusteijn, T. 1996, A&A, 314, 484
Díaz Trigo, M., Migliari, S., Miller-Jones, J. C. A., & Guainazzi, M. 2014, A&A, 571, A76
Done, C., Gierliński, M., & Kubota, A. 2007, A&ARv, 15, 1
Dovčiak, M., Muleri, F., Goosmann, R. W., Karas, V., & Matt, G. 2008, MNRAS, 391, 32
Dumont, A.-M., Collin, S., Paletou, F., et al. 2003, A&A, 407, 13
Esin, A. A., McClintock, J. E., & Narayan, R. 1997, ApJ, 489, 865
Fender, R. P. 2001, MNRAS, 322, 31
Ferland, G. J., Chatzikos, M., Guzmán, F., et al. 2017, RMxAA, 53, 385
Ferreira, J. 1997, A&A, 319, 340
Fukumura, K., Kazanas, D., Contopoulos, I., & Behar, E. 2010, ApJ, 715, 636
Fukumura, K., Kazanas, D., Shrader, C., et al. 2021, ApJ, 912, 86
Gendreau, K. C., Arzoumanian, Z., Adkins, P. W., et al. 2016, Proc. SPIE, 9905, 99051H
Giacconi, R., Murray, S., Gursky, H., et al. 1972, ApJ, 178, 281
Gierliński, M., Zdziarski, A. A., Poutanen, J., et al. 1999, MNRAS, 309, 496
Goosmann, R. W., & Gaskell, C. M. 2007, A&A, 465, 129
Harrison, F. A., Craig, W. W., Christensen, F. E., et al. 2013, ApJ, 770, 103
Hubeny, I., & Hubeny, V. 1998, ApJ, 505, 558
Hubeny, I., Hummer, D. G., & Lanz, T. 1994, A&A, 282, 151
Ingram, A., Bollemeijer, N., Veledina, A., et al. 2023, arXiv:2311.05497
Jiang, J., Tomsick, J., Liu, H., et al. 2022, ATel, 15575, 1
Joye, W. A., & Mandel, E. 2003, in ASP Conf. Ser. 295, Astronomical Data Analysis Software and Systems XII, ed. H. E. Payne, R. I. Jedrzejewski, & R. N. Hook (San Francisco, CA: ASP), 489
Kaastra, J. S., & Bleeker, J. A. M. 2016, A&A, 587, A151
Kalemci, E., Maccarone, T. J., & Tomsick, J. A. 2018, ApJ, 859, 88
King, A. L., Walton, D. J., Miller, J. M., et al. 2014, ApJL, 784, L2
Krawczynski, H., Muleri, F., Dovčiak, M., et al. 2022, Sci, 378, 650
Kushwaha, A., Jayasurya, K. M., Agrawal, V. K., & Nandi, A. 2023, MNRAS, 524, L15
Kuulkers, E., Wijnands, R., Belloni, T., et al. 1998, ApJ, 494, 753
Li, L.-X., Zimmerman, E. R., Narayan, R., & McClintock, J. E. 2005, ApJS, 157, 335
Lightman, A. P., & Shapiro, S. L. 1975, ApJL, 198, L73
Loskutov, V. M., & Sobolev, V. V. 1979, Afz, 15, 241
Loskutov, V. M., & Sobolev, V. V. 1981, Afz, 17, 97
Marin, F. 2018, A&A, 615, A171
Marin, F., Goosmann, R. W., Gaskell, C. M., Porquet, D., & Dovčiak, M. 2012, A&A, 548, A121
Marin, F., Goosmann, R. W., & Gaskell, C. M. 2015, A&A, 577, A66
Marra, L., Brigitte, M., Rodriguez Cavero, N., et al. 2023, arXiv:2310.11125
Matsuoka, M., Kawasaki, K., Ueno, S., et al. 2009, PASJ, 61, 999
McClintock, J. E., & Remillard, R. A. 2006, in Compact Stellar X-Ray Sources, ed. W. Lewin & M. van der Klis (Cambridge: Cambridge Univ. Press), 157
Mészáros, P., & Rees, M. J. 1997, ApJL, 482, L29
Mikusincova, R., Dovciak, M., Bursa, M., et al. 2023, MNRAS, 519, 6138
Miller, J. M., Fabian, A. C., Kaastra, J., et al. 2015, ApJ, 814, 87
Milne, E. A. 1921, MNRAS, 81, 361
Nasa High Energy Astrophysics Science Archive Research Center, HEASARC 2014, HEAsoft: Unified Release of FTOOLS and XANADU, Astrophysics Source Code Library, record, ascl:1408.004
Novikov, I. D., & Thorne, K. S. 1973, in Black Holes, ed. C. DeWitt & B. DeWitt (London: Gordon and Breach), 343
Page, D. N., & Thorne, K. S. 1974, ApJ, 191, 499
Parmar, A. N., Stella, L., & White, N. E. 1986, ApJ, 304, 664
Podgorný, J., Dovčiak, M., Marin, F., Goosmann, R., & Różańska, A. 2022, MNRAS, 510, 4723
Podgorný, J., Marra, L., Muleri, F., et al. 2023, MNRAS, 526, 5964
Ponti, G., Fender, R. P., Begelman, M. C., et al. 2012, MNRAS, 422, L11
Poutanen, J., Veledina, A., & Beloborodov, A. M. 2023, ApJL, 949, L10
Priedhorsky, W. 1986, Ap&SS, 126, 89
Ramsey, B. D., Bongiorno, S. D., Kolodziejczak, J. J., et al. 2019, Proc. SPIE, 11119, 1111903
Ratheesh, A., Matt, G., Tombesi, F., et al. 2021, A&A, 655, A96
Rawat, D., Garg, A., & Méndez, M. 2023, ApJL, 949, L43
Reid, C. A., Johnston, M. D., Bradt, H. V., et al. 1980, AJ, 85, 1062
Remillard, R. A., Loewenstein, M., Steiner, J. F., et al. 2022, AJ, 163, 130
Remillard, R. A., & McClintock, J. E. 2006, ARA&A, 44, 49
Riffert, H., & Herold, H. 1995, ApJ, 450, 508
Rodriguez Cavero, N., Marra, L., Krawczynski, H., et al. 2023, ApJL, 958, L8
Sądowski, A. 2011, arXiv:1108.0396
Schnittman, J. D., & Krolik, J. H. 2009, ApJ, 701, 1175
Seifina, E., Titarchuk, L., & Shaposhnikov, N. 2014, ApJ, 789, 57
Shakura, N. I., & Sunyaev, R. A. 1973, A&A, 24, 337
Sobolev, V. V. 1963, A Treatise on Radiative Transfer (Princeton, NJ: Van Nostrand-Reinhold)
Soffitta, P., Baldini, L., Bellazzini, R., et al. 2021, AJ, 162, 208
Stark, R. F., & Connors, P. A. 1977, Natur, 266, 429
Straub, O., Bursa, M., Sądowski, A., et al. 2011, A&A, 533, A67
Suleimanov, V. F., Ghosh, K. K., Austin, R. A., & Ramsey, B. D. 2002, AstL, 28, 745
Suleimanov, V. F., Lipunova, G. V., & Shakura, N. I. 2007, ARep, 51, 549
Suleimanov, V. F., Poutanen, J., Doroshenko, V., & Werner, K. 2023, A&A, 673, A15
Suleymanov, V. F. 1992, SvAL, 18, 104
Svoboda, J., Dovčiak, M., Steiner, J. F., et al. 2024, ApJ, 960, 3
Taverna, R., Marra, L., Bianchi, S., et al. 2021, MNRAS, 501, 3393
Taverna, R., Zhang, W., Dovčiak, M., et al. 2020, MNRAS, 493, 4960
Tomaru, R., Done, C., & Odaka, H. 2024, MNRAS, 527, 7047
Tomsick, J. A., Corbel, S., Goldwurm, A., & Kaaret, P. 2005, ApJ, 630, 413
Tomsick, J. A., Lapshov, I., & Kaaret, P. 1998, ApJ, 494, 747
Veledina, A., Muleri, F., Dovčiak, M., et al. 2023a, ApJL, 958, L16
Veledina, A., Muleri, F., Poutanen, J., et al. 2023b, arXiv:2303.01174
Wang, J., Mastroserio, G., Kara, E., et al. 2021, ApJL, 910, L3
Weisskopf, M. C., Soffitta, P., Baldini, L., et al. 2022, JATIS, 8, 026002
West, A., & Krawczynski, H. 2023, ApJ, 957, 9
Wielgus, M., Lančová, D., Straub, O., et al. 2022, MNRAS, 514, 780
Wilms, J., Allen, A., & McCray, R. 2000, ApJ, 542, 914
Zdziarski, A. A., Grove, J. E., Poutanen, J., Rao, A. R., & Vadawale, S. V. 2001, ApJL, 554, L45
Zdziarski, A. A., Johnson, W. N., & Magdziarz, P. 1996, MNRAS, 283, 193
Zimmerman, E. R., Narayan, R., McClintock, J. E., & Miller, J. M. 2005, ApJ, 618, 832
Życki, P. T., Done, C., & Smith, D. A. 1999, MNRAS, 309, 561